JOURNAL OF GEOPHYSICAL RESEARCH, VOL. 104, NO. C11, PAGES 25,833–25,851, NOVEMBER 15, 1999

A case study of air-sea interaction during swell conditions

A. Smedman, U. Högström, H. Bergström, and A. Rutgersson
Department of Earth Sciences, Meteorology, University of Uppsala, Uppsala, Sweden

K. K. Kahma and H. Pettersson
Finnish Institute of Marine Research, Helsinki

Abstract. Air-sea interaction data from a situation with pronounced unidirectional swell have been analyzed. Measurements of turbulence at three levels (10, 18, and 26 m above mean sea level) together with directional wave buoy data from the site Östergarnsholm in the Baltic Sea were used. The situation, which lasted for ~48 hours, appeared in the aftermath of a gale. The wind direction during the swell situation turned slowly within a 90° sector. Both during the gale phase and the swell phase the over-water fetch was >150 km. The wind speed during the swell phase was typically 4 m s^{-1}. During the swell phase a wind maximum near or below the lowest wind speed measuring level 10 m was observed. The net momentum flux was very small, resulting in C_D values ~0.7×10^{-3}. Throughout the lowest 26 m, covered by the tower measurements, turbulence intensities in all three components remained high despite the low value of the kinematic momentum flux $-\overline{u'w'}$, resulting in a reduction of the correlation coefficient for the longitudinal and vertical velocity from its typical value around −0.35 to between −0.2 and 0 (and with some positive values at the higher measuring levels), appearing abruptly at wave age c_0/U_{10} equal to 1.2. Turbulence spectra of the horizontal components were shown not to scale with height above the water surface, in contrast to vertical velocity spectra for which such a variation was observed in the low-frequency range. In addition, spectral peaks in the horizontal wind spectra were found at a frequency as low as 10^{-3} Hz. From a comparison with results from a previous study it was concluded that this turbulence is of the "inactive" kind, being brought down from the upper parts of the boundary layer by pressure transport.

1. Introduction

The air-sea interaction regime characterized by the dominating waves traveling faster than the wind (swell) is much less well studied and understood than the situation with a wind speed higher than the dominant wave speed. In view of obvious applications the interest in situations with growing waves is natural. Nevertheless, as pointed out already by *Kitaigorodskii* [1973], possible widespread occurrence of "supersmooth flow" [*Donelan*, 1990] over the ocean could be of considerable interest from a global climatological viewpoint. Observations of situations with very low surface friction and even, sometimes, momentum flux directed from the water surface to the atmosphere during conditions with $c_0/U > 1$, where c_0 is the speed of the dominating waves and U is the wind speed at some low height above the water surface (typically 10 m), were made during several marine Soviet expeditions in the 1970s [*Volkov*, 1970; *Makova*, 1975; *Benilov et al.*, 1974]. Similar results were reported from measurements over Lake Michigan by *Davidson and Frank* [1973] and from waters outside the Australian coast by *Antonia and Chambers* [1980] and *Chambers and Antonia* [1981]. *Smedman et al.* [1994] (hereinafter referred to as STH (1994)) carried out an intensive study of the entire marine boundary layer with the aid of an instrumented aircraft and tower-mounted instrumentation during a situation with no surface shearing stress at a site in the Baltic Sea. The near-surface atmospheric characteristics in the STH (1994) study were very much the same as those reported in the above-cited references. No wave measurements were available, but as the situation appeared in the aftermath of a gale, it was conjectured that "swell conditions," here defined as conditions with $c_0/U_{10} \geq 1.2$, prevailed.

Paper number 1999JC900213.
0148-0227/99/1999JC900213$09.00

The basic conceptual idea for air-sea interaction during swell conditions is that the surface waves transport momentum upward into the atmosphere, with the aid of pressure fluctuations induced by the waves. That this actually occurs, at least during idealized laboratory conditions over mechanically generated monochromatic waves, has been convincingly demonstrated in several studies [*Harris*, 1966; *Lai and Shemdin*, 1971]. The depth of the atmospheric layer affected by this energy transfer was found by *Lai and Shemdin* [1971] to be appreciable and much deeper than the corresponding depth affected in the case of developing waves (when there is a pressure transport of energy in the opposite direction, i.e., from the atmosphere to the water surface). The field studies reported by *Makova* [1975] seem, in fact, to indicate that surface wave–induced signatures can be traced to appreciable heights in those conditions.

The laboratory studies cited above were conducted over monochromatic waves, giving rise to a well-defined peak in spectra of the wind components at the same frequency. With a natural oceanic wave spectrum, wave forcing occurs over a continuum in frequency. *Benilov et al.* [1974] carried out a theoretical analysis based on a simplified assumption of the interaction of turbulence in the airflow with the wave-induced

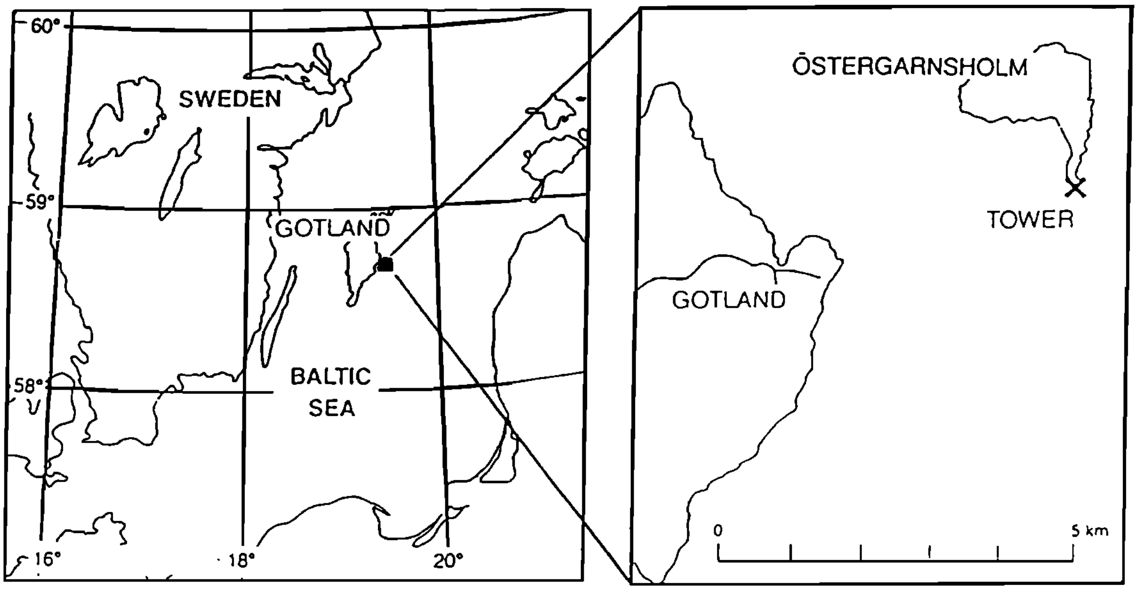

Figure 1. Map of the Baltic Sea, with a close-up of the site Östergarnsholm. The wave buoy is moored in 36 m deep water ~4 km to the ESE of the tower site on Östergarnsholm, having roughly the same sector of >150 km unobstructed over-water fetch as the tower site.

perturbations and arrived at spectral transfer functions that result in appreciable influences over a broad band of frequencies, particularly so for the swell case and for the spectrum of vertical velocity. Although *Belcher and Hunt* [1993] convincingly show that the key assumption made by *Benilov et al.* [1974], i.e., that the "basic" turbulent fluctuations of the airflow over the waves are passively advected along wavy trajectories, is fundamentally wrong for the case of strongly developing waves, the situation related to swell conditions in this respect is not known.

In spring 1995 an air-sea interaction research facility for long-term measurements of turbulent fluxes at three levels above the water surface and simultaneous surface wave measurements was established at a site in the Baltic Sea called Östergarnsholm. The measurements and the site are described in section 2. From the data set available from this site so far, a particular situation, occurring on September 18–19, 1995, has been chosen for an analysis of the air-sea interaction mechanism during swell conditions. As described in section 3, this situation occurred during a period immediately following a gale, which culminated during September 15 and 16, resulting in low winds and swell, so that $c_0/U_{10} \geq 1.2$. In section 4 the turbulence structure is presented. In section 5 the findings are discussed with reference to previous findings in general and those reported by STH (1994) in particular.

2. Site and Measurements

The main measuring site is the island Östergarnsholm, situated ~4 km east of the big island of Gotland in the Baltic Sea, Figure 1. Östergarnsholm is a low island with no trees. The 1 km long peninsula in the southeastern part of the island rises to no more than a couple of meters above mean sea level. A 30 m tower has been erected at the southernmost tip of this peninsula. The base of the tower is situated at just about 1 m above mean sea level. The distance from the tower to the shoreline in calm conditions is only a few tens of meters in the sector from NE to SW in the clockwise sense. The seafloor up to 500 m from the peninsula has an approximate slope of 1:30, varying somewhat in different directions. About 10 km from the peninsula, the depth is 50 m, reaching below 100 m farther out. In section 3 the possible influence of limited depth on the wave field is discussed.

The data from a wave rider buoy (run and owned by the Finnish Institute for Marine Research) moored at 36 m depth ~4 km from the tower in the direction 115° represent the wave conditions in the upwind fetch. During the swell period the buoy is exposed to nearly the same general wave conditions as the flux measurements.

The 30 m tower is instrumented with slow-response ("profile") sensors of in-house design for temperature [*Högström*, 1988] and for wind speed and direction [*Lundin et al.*, 1990] at the following heights above the tower base: 7, 11.5, 14, 20, and 28 m. In addition, humidity was measured at 7 m above the tower base. Turbulent fluctuations were recorded with SOLENT 1012R2 sonic anemometers (Gill Instruments, Lymington, United Kingdom) at the heights of 9, 17, and 25 m above the tower base. The sonics were calibrated individually in a big wind tunnel prior to being installed on the tower. The calibration procedure used is similar to that described by *Grelle and Lindroth* [1994], giving a matrix of calibration constants which correct for flow distortion caused by the instrument itself. From the sonic signals the three orthogonal components of the wind and virtual temperature (the measured temperature signal agrees to within 0.20% with the virtual temperature [*Depuis et al.*, 1997]) are obtained.

Both profile and turbulence data are 1 hour averages. In order to remove possible trends, a high-pass filter based on a 10 min running average was applied to the turbulence time series prior to calculating moments (variances and covariances). This procedure amounts to applying a high-pass filter with a cutoff frequency at $\sim 10^{-3}$ Hz. A way to check that this procedure does not mean reducing the measured variances and covariances is to produce so-called ogive curves, i.e., to integrate measured cospectra (derived from the unfiltered time series) from the high-frequency end (in this case 10 Hz) to successively lower frequencies n and plot this integral as a function of n. The result is a curve which normally rises monotonically with decreasing frequency and which finally levels out asymptotically. This asymptote gives the total covariance. For the swell cases of this study it is found that the ogives attain a plateau at a frequency somewhere in the range $2 \times 10^{-3} < n < 10^{-2}$ Hz and then rise to a final asymptote at $n \approx 10^{-3}$ Hz. These two plateaus are likely to represent different transport mechanisms. Nevertheless, we have used the low-frequency plateau throughout to obtain an estimate of the total flux. This means that our 10 min running mean procedure gives accurate representation of the covariances and hence of the corresponding fluxes.

As discussed in section 5, the low-frequency part of the turbulence during swell is likely to be highly influenced by so-called "inactive" turbulence, brought down by pressure transport from the upper layers of the boundary layer to the layers near the surface. This turbulence does not contribute to the momentum flux but causes random variability in the low-frequency part of the u, w cospectrum, where u and w are the longitudinal and vertical components, respectively. This is the cause of the large scatter in the plots involving the kinematic momentum flux $-\overline{u'w'}$.

The measurements run continuously, with a sampling frequency of 1 Hz for the meteorological slow-response (profile) sensors and 20 Hz for the turbulence signals. Wave data is recorded once an hour. The directional spectrum is calculated from 1600 s of data onboard the buoy. The spectrum has 64 frequency bands (0.025–0.58 Hz). The significant wave height is calculated by trapezoid method from frequency bands 0.05–0.58 Hz, and the peak frequency is determined by a parabolic fit. The meteorological measurements have been running semi-continuously from May 1995. Wave data have been recorded semi-continuously during the same period but with breaks during wintertime periods with risk for ice damage.

For the present analysis of swell, data have been chosen from one particular situation, September 18–19, 1995, with due reference also to the high-wind period preceding the swell situation itself, as described in detail in section 3.

3. General Characteristics of the Measuring Situation

Figure 2a shows, for the time period September 14–19, 1995, the variation of the wind speed (stars and left-hand scale) and significant wave height (circles and right-hand scale), Figure 2b presents wind direction and dominant wave direction, and Figure 2c gives the phase speed of the dominating wave. The wind increased at first to a maximum of ~16 m s^{-1} on September 15, followed by a decrease to ~4 m s^{-1} on September 18 and 19. The wind direction (Figure 2b, stars) during the period September 14–17 was ~90°, turning to between 110° and 200° during the last two days of the period. With reference to the description of the site in section 2 it is clear that the wind was from the sector where the upwind fetch was over 150 km. As previously stated, the present study will concentrate on results from the last 2 days. The phase speed plot, Figure 2c, shows both the phase speed of dominant waves in deep water (stars), which is expected to equal the deep-water value, and a weighted mean phase speed $\langle c_0 \rangle$ that represents the phase speed of dominant waves in the footprint, calculated over the flux footprint of the 10 m measurements (circles) (see appendices A and B) and the 26 m measurements (crosses), with the limited depth being accounted for.

From Figure 2c we can see that $\langle c_0 \rangle$ for the footprint of turbulent flux measured at 26 m height (the crosses) does not differ noticeably from the deep-water phase speed (the stars), except during a short time at the very peak of the gale. As shown in the so-called footprint analysis in appendix A, during typical conditions, 90% of the turbulent flux measured at 26 m height originates from distances >770 m away from the tower. At lower levels the footprint of the turbulent flux lies closer to the tower and partly in shallower water. Still, Figure 2c shows that during the swell period, $\langle c_0 \rangle$, over all the footprints corresponding to the measurement heights 10 m and 26 m, is very close to the deep-water value of c_0. This applies also to the period before the gale.

Using the results of *Anctil and Donelan* [1996], we have estimated in appendix B that the reduction in $\langle c_0 \rangle$ (compared with the deep-water value) should be larger than that seen in Figure 2c before shoaling wave effects manifest themselves in the airflow. This result is confirmed in the analysis of turbulence moments presented in section 4.2, where no distinction is found in the plots for cases where $\langle c_0 \rangle$ is very close to the deep-water value. It is also shown that the results of the analysis are, in effect, independent of measuring height and thus of differences in footprint.

Our conclusion, therefore, is that during the swell period it is very unlikely that the turbulent flux measurements at any of the three levels are influenced by effects of limited water depth. During the gale these effects seem small, and they cannot alter the significant differences observed between the swell period and the pre-swell period.

While multiple peaks are common in wave spectra in the Baltic Sea, especially during swell, the wave spectra during the study period exhibit only one well-defined peak. A typical example of a measured spectrum is presented in Figure 3 (the top curve). Also shown in Figure 3 is the corresponding Pierson-Moskowitz spectrum [*Pierson and Moskowitz*, 1964] calculated for the same wind speed, 4 m s^{-1}, as that measured locally. Figure 3 shows that swell energy dominates the spectrum, and up to 0.6 Hz, the wave spectrum is higher than the maximum spectrum that can be generated by the local wind. The swell has been generated several hours earlier ~100 km to the south by the higher wind that was blowing at that time. By the time the waves arrived at the measuring point the wind had decayed, and the waves had turned into swell. The shorter local waves (the shaded spectrum in Figure 3) were generated by the weaker local wind from the SE. The directional spreading between 0.27 and 0.5 Hz is therefore higher than normal. This confirms that at those frequencies the spectrum is the sum of the two wave systems: the fully developed local waves and the superimposed swell. During September 18 and 19 there were periods when wind and wave directions were very close (Figure 2b) but also periods with deviations as large as 60°. In the analyses presented in section 4.2, data from this period have been divided into two groups according to whether the deviation between wind and wave direction is less than or larger than 30°.

Figure 4 shows the wind gradient evaluated at 10 m (in the following text, "height" always refers to height above mean sea level) for the entire period September 14–19. The gradient was derived at the lowest turbulence level, 10 m, from a best fit

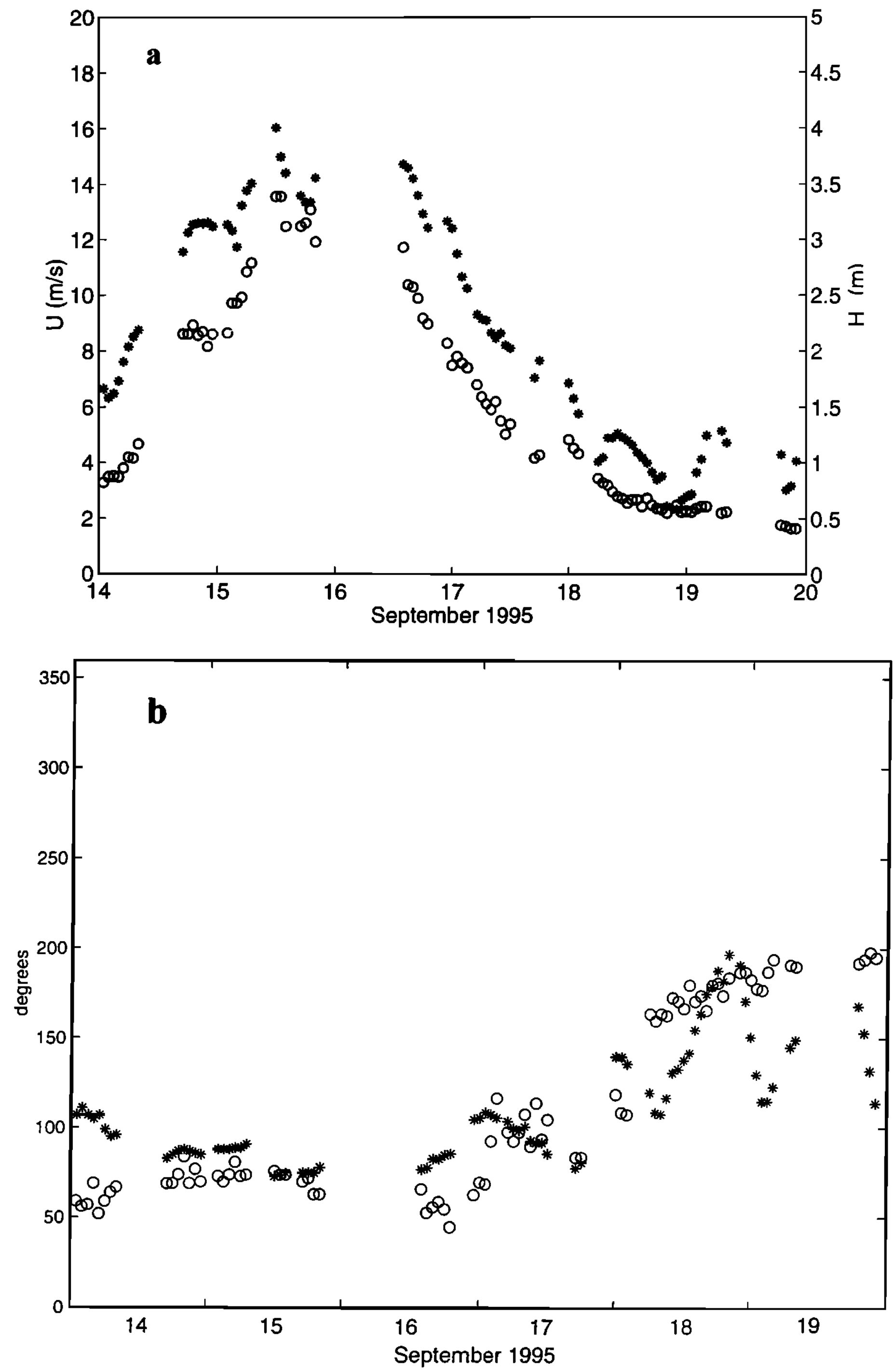

Figure 2. (a) Hourly mean wind speed U at 10 m above mean sea level, denoted by stars, and significant wave height H_s, denoted by circles, during the time period September 14–19, 1995. (b) Wind direction at 10 m, denoted by stars, and dominant wave direction, denoted by circles, during the same time period as in Figure 2a. (c) Phase speed of dominant waves c_0. Deep-water values are denoted by stars, and weighted mean values over the flux footprint are denoted for the 10 m measurements by circles and for the 26 m measurements by crosses (see appendix B for details).

log-lin plot of wind speed measured at the five heights mentioned in section 2. Note that the gradient is negative for most of the time during September 18–19. This means that the wind profile has a maximum at a height below 10 m. It is natural to interpret this local wind speed increase as the effect of a "wave-driven wind"; compare the laboratory result of *Harris* [1966] and the field result from Lake Ontario of *Donelan* [1990].

The kinematic momentum flux $-\overline{u'w'}$ drops to very small values (around or below 0.01 $m^2\ s^{-2}$) at ~2000 local standard time (LST) on September 17 and stays at that low level for the remaining period. As noted above, the wind gradient becomes negative or very small at the same time as the momentum flux drops to values near zero.

Stability was close to neutral during the high-wind period

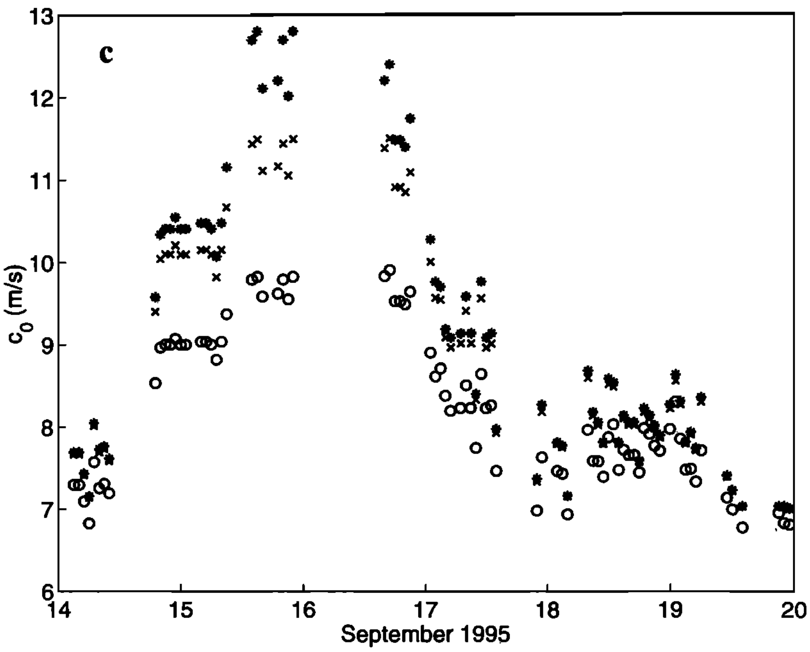

Figure 2. (continued)

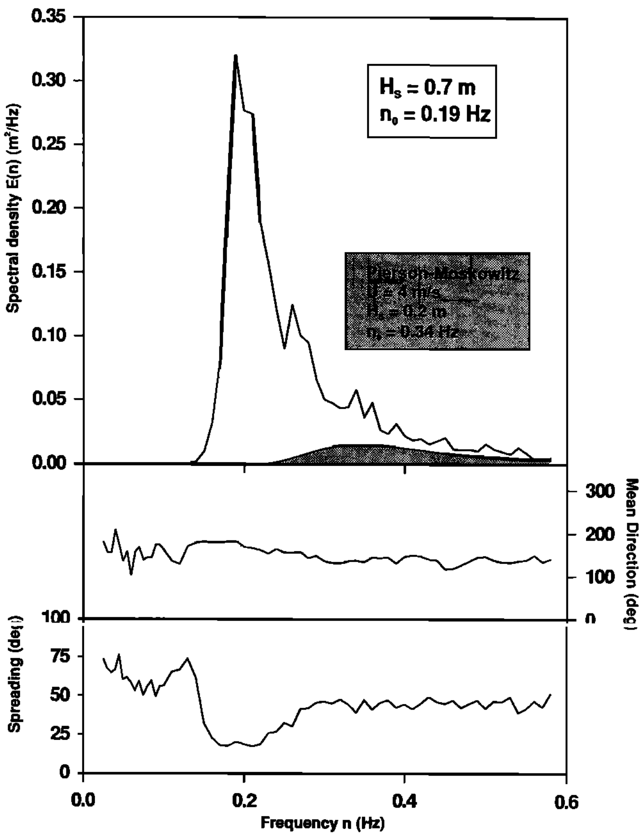

Figure 3. An example of wave spectrum with mean direction and spreading versus frequency during the swell period. The smaller shaded spectrum is the Pierson-Moskowitz spectrum [*Pierson and Moskowitz*, 1964] for fully developed waves at 4 m s^{-1} wind speed, the local wind speed during the measurement.

(September 14–17). During September 18–19 the sensible heat flux was positive but numerically small. As discussed in section 5, it is doubtful whether it is meaningful to attempt a stability correction during those conditions. Calculation of C_D for the swell period gives a mean of ~0.7 × 10^{-3}, with large scatter. Here C_D is defined in the usual manner as $C_D = (u_*/U_{10})^2$, where U_{10} is wind speed at 10 m.

In Figure 5, hourly mean values of the vertical wind gradient at 10 m (derived from 5 levels of wind speed measurements) have been plotted as a function of wind speed for the same height for the entire time period of wind increase and subsequent decrease (compare Figure 2). The curves with arrows drawn by hand to fit the data indicate the direction of evolution with time. A pronounced hysteresis effect is found. Thus during the stage of increasing wind a wind speed of 7 m s^{-1} corresponds to a wind gradient of ~0.05 s^{-1}, as compared to a value of just 0.01 s^{-1} for the same wind speed during decreasing wind conditions. Again, it is seen in this plot that the wind gradient becomes negative for most of the time during September 18 and 19.

4. Turbulence Characteristics

4.1. Turbulence Kinetic Energy Budget

In stationary and horizontally homogeneous conditions the turbulence kinetic energy budget (the TKE budget) attains the form [*Monin and Yaglom*, 1971]:

$$\overline{u'w'}\frac{\partial U}{\partial z} - \frac{g}{T_0}\overline{w'\theta_v'} + \frac{\partial}{\partial z}\frac{\overline{w'e'^2}}{2} + \frac{1}{\rho_0}\frac{\partial}{\partial z}\overline{p'w'} + \bar{\varepsilon} = 0, \quad (1)$$

$$P \qquad B \qquad T_t \qquad T_p \qquad \varepsilon$$

where $\overline{e^2/2} = \frac{1}{2}(u^2 + v^2 + w^2)$ is the turbulent kinetic energy, $-\overline{u'w'}$ is the kinematic momentum flux, $\overline{w'\theta_v'}$ is the

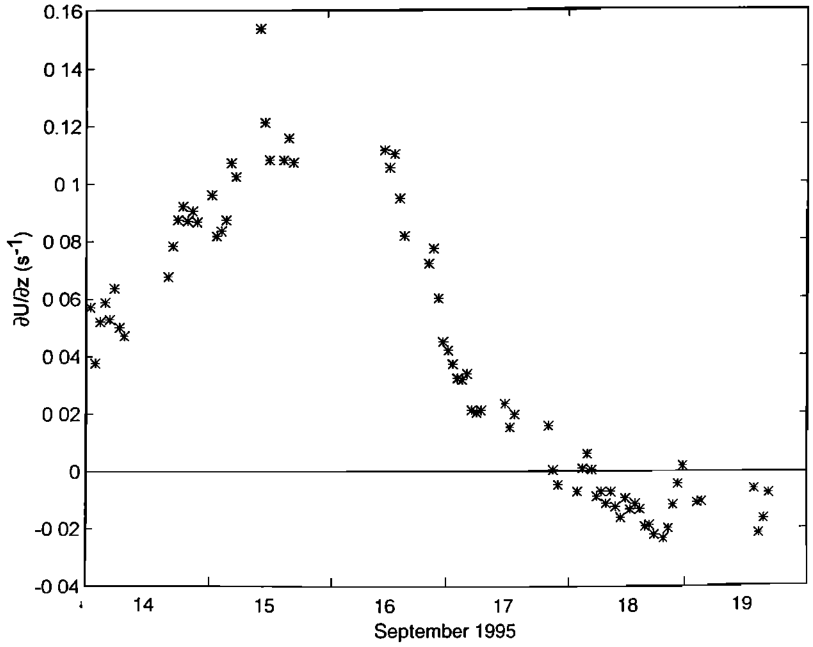

Figure 4. Wind gradient at 10 m, derived from cup anemometer measurements at five levels for the time period September 14–19, 1995. Note that negative gradients prevail during most of the swell period, September 18–19.

kinematic heat flux, or, more precisely, the flux of virtual potential temperature. T_0, mean temperature (in Kelvin) of the surface layer; g, acceleration due to gravity; ρ_0, air density at temperature T_0. The physical interpretation of the various terms in (1) is as follows: P, mechanical production of TKE from the mean flow; $B = -(g/T_0)(\overline{w'\theta'_v})$, production ($B < 0$) or destruction ($B > 0$) of TKE by buoyancy; T_t, turbulent transport of TKE; T_p, pressure transport of TKE; and ε, molecular rate of dissipation of TKE.

Figure 6 shows the terms of the TKE budget for the time period with swell, September 18–19, 1995. The terms P and B were evaluated from the turbulence measurements at 10 m and

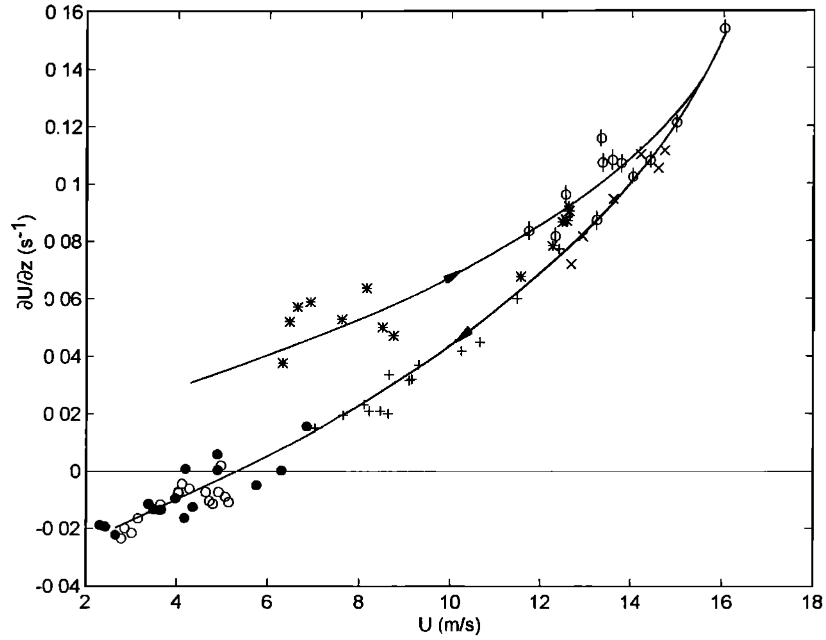

Figure 5. Estimated values of hourly mean wind speed gradient at 10 m (determined from cup anemometer measurements at five levels) for the entire time period September 14–19, 1995, plotted as a time sequence in the direction indicated by the arrows and as a function of wind speed at 10 m. Stars, September 14; phis, September 15; crosses, September 16; pluses, September 17; solid circles, September 18; and open circles, September 19.

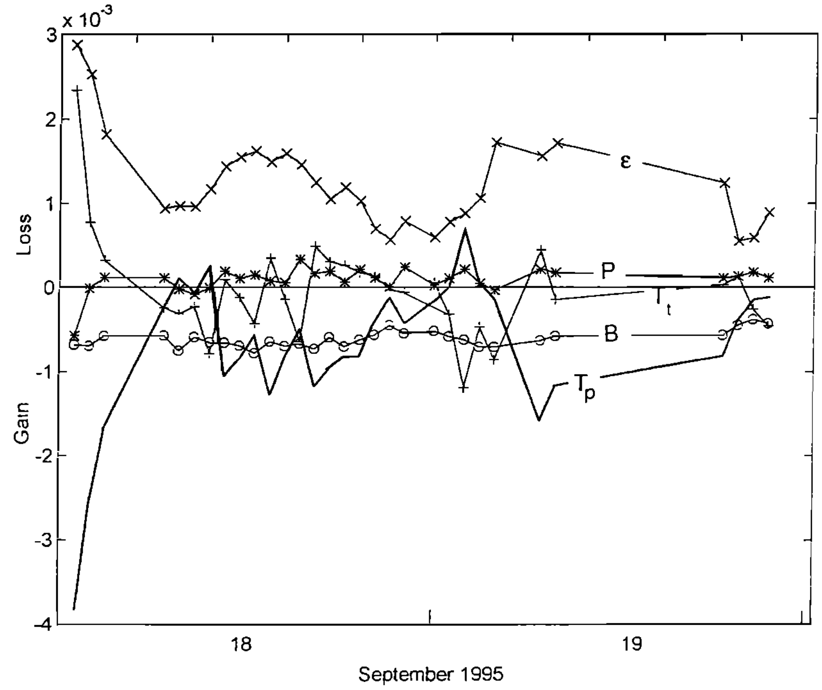

Figure 6. Turbulence energy budget at 10 m for the time period with swell, September 18–19, 1995. B, buoyancy production; P, mechanical production; ε, dissipation; T_p, pressure transport term; and T_t, turbulent transport term. Values are to the 10^{-3} power.

from mean wind profile fits. The turbulence transport term T_t was derived from measurements of $\overline{w'e'^2}$ at the levels 10 and 18 m. The dissipation term ε was obtained from inertial subrange levels of longitudinal velocity spectra, assuming a value of 0.52 for the Kolmogoroff spectral constant α [*Högström*, 1990]. The pressure transport term T_p was assumed to equal the imbalance. This is a reasonable assumption, considering that changes in the turbulence energy were sometimes positive and sometimes negative, with no indication of a systematic time rate of change during the time period of swell studied here; nor were any systematic advective changes observed. Concerning interpretation of the pressure transport term, see section 5.

From Figure 6 it is first of all seen that mechanical production of turbulent kinetic energy is close to zero during the entire period. The two dominating source terms are buoyancy production B and pressure transport T_p. The following mean values are obtained for the entire swell period, September 18–19, 1995: $P = 0.08 \times 10^{-3}$ m^2 s^{-3}, $T_p = -0.47 \times 10^{-3}$ m^2 s^{-3}, $T_t = -0.10 \times 10^{-3}$ m^2 s^{-3}, $B = -0.62 \times 10^{-3}$ m^2 s^{-3}, and $\varepsilon = 1.11 \times 10^{-3}$ m^2 s^{-3}.

4.2. Turbulence Moments

The correlation coefficient between u and w is defined

$$r_{uw} = \overline{u'w'}/\sigma_u\sigma_w, \qquad (2)$$

where $-\overline{u'w'} = u_*^2$, the kinematic momentum flux; σ_u, the standard deviation of the longitudinal wind component; and σ_w, the standard deviation of the vertical wind component.

Figure 7a shows, for 10 m, r_{uw} plotted against wave age c_0/U_{10} (actually, $\langle c_0/U_{10}\rangle$, where angle brackets denote the weighted mean, but for convenience we drop the angle brackets from here on). During the period September 14–17 when $c_0/U_{10} < 1.2$ the correlation coefficient has its usual value found in near-neutral atmospheric surface layers over land, -0.35 ± 0.05. For swell conditions of the last two days, r_{uw} attains values between -0.20 and 0. Note the rapid transition in the value of r_{uw} at $c_0/U_{10} = 1.2$, the wave age at which the waves become fully developed according to *Pierson and Moskowitz* [1964]. As illustrated by the mean values presented in Table 1, the situation is exactly the same at 18 and at 26 m; see also Figure 7b, which shows the situation for the 26 m level. The observed trend of r_{uw} with wave age is in agreement with earlier findings, i.e., *Kitaigorodskii* [1973] and *Makova* [1975]. Most previous studies of this quantity were, however, made at a fairly low height above the water surface. Note that there is no significant difference between the two groups during the swell period representing small and large deviation between wind and wave direction, nor do the data points representing "pregale conditions" (circles) stand out among the other data for "young wave conditions." The reason for the drop of $-r_{uw}$ with wave age is very probably the dominance of so-called inactive turbulence during swell, as discussed in detail in section 5.

Figure 8 shows, for 10 m, σ_w/u_* as a function of c_0/U_{10}. As illustrated by the mean values presented in Table 2, the result is very much the same for the other two measuring heights, 18 and 26 m. This quantity has its normal neutral value of ~1.2 for $c_0/U_{10} < 1.2$ and values about double that for swell conditions. Again, note the rapid transition at the fully developed wave age $c_0/U_{10} = 1.2$. Also, in this plot there is no systematic difference between swell cases with small and large deviation between wind and wave direction or for the pregale data during the phase with $c_0/U_{10} < 1.2$. Exactly similar increases as for σ_w/u_* are found for the normalized standard deviations of the two horizontal components, σ_u/u_* and σ_v/u_* (not

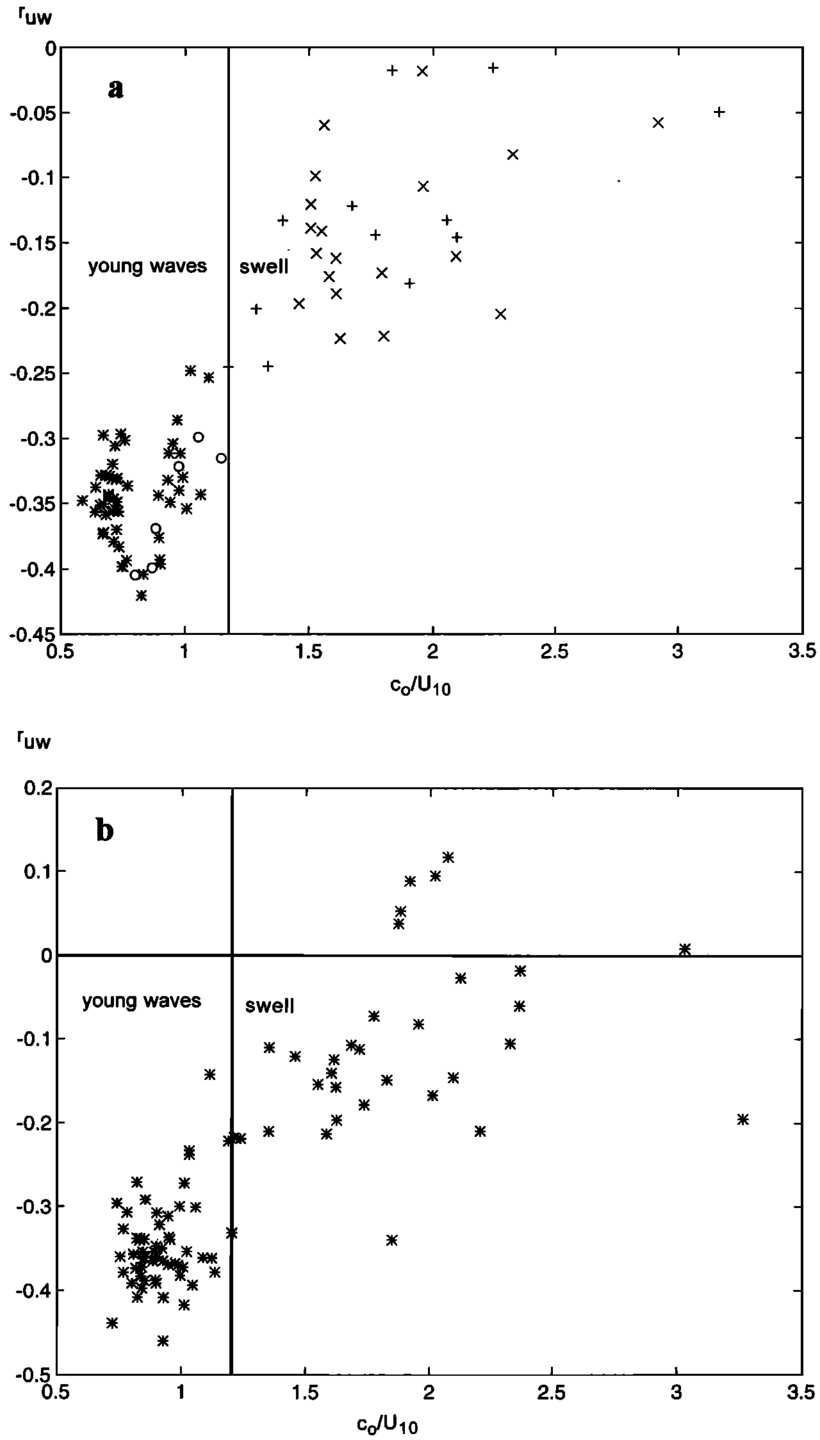

Figure 7. (a) Correlation coefficient $r_{uw} = \overline{u'w'}/(\sigma_u \sigma_w)$ for 10 m plotted as a function of the wave age parameter c_0/U_{10} (where c_0 has been calculated as weighted means over the flux footprint for the 10 m level, see appendix B). Circles, data from the pregale period during September 14; stars, data from the gale period September 14–17; pluses, data from September 18 and 19, with wind-wave angle difference ≤30°; crosses, same as pluses, but with wind-wave angle difference between 30° and 60°. (b) Same as Figure 7a but from measurements at 26 m and with c_0 calculated as weighted means over the flux footprint for this level. Note that here no distinction is made between the three data categories of Figure 7a.

shown here). Thus the normalized turbulence energy increases by a factor of 3 to 4 for $c_0/U_{10} > 1.2$ compared to its normal value. In section 5 it is explained how this result is a consequence of the flow being dominated by inactive turbulence.

4.3. Spectral Characteristics

In a near-neutral surface layer over land, spectra of atmospheric variables scale linearly with the height above the surface [*Kaimal et al.*, 1972]. During the period of increasing wind

Table 1. Mean Values and Standard Deviations for the Correlation r_{uw} for the Three Measuring Heights and for Young Waves ($c_0/U_{10} < 1.2$) and Swell ($c_0/U_{10} > 1.2$)

	10 m			18 m			26 m		
	r_{uw}	s.d.	N	r_{uw}	s.d.	N	r_{uw}	s.d.	N
$c_0/U_{10} < 1.2$	−0.34	0.04	57	−0.38	0.05	57	−0.34	0.05	57
$c_0/U_{10} > 1.2$	−0.14	0.07	33	−0.17	0.07	33	−0.10	0.11	33

N, number of measuring hours for each category.

in September 1995 this was also found to be the case for spectra measured at Östergarnsholm (not shown here). Such scaling is not obtained during the swell period. Figure 9 shows an example of the longitudinal velocity spectrum $nS_u(n)$, where n is frequency, plotted against n for the three measuring heights 10, 18, and 26 m. It is clear that the spectra are virtually independent of height (the points representing the two lowest frequencies being very uncertain, for statistical reasons). An exactly similar picture is obtained for the spectrum of the lateral component $nS_v(n)$ (not shown here). The spectrum for the vertical component $nS_w(n)$ differs in a systematic way from this picture, as shown in Figure 10. For this component the high-frequency part of the spectrum (above $n \approx 0.1$ Hz) is also independent of height. The spectral level of the low-frequency part varies, however, systematically with height. The present result for the horizontal and vertical velocity spectra is in total agreement with the findings from measurements throughout the boundary layer in the study by STH (1994), as discussed in detail in section 5.

Twenty-four hour mean u, v, and w spectra are shown in Figure 11. Possible weak wave influences may be noted. Thus the vertical velocity spectrum has a wide plateau, and the horizontal velocity spectra have an inflection or even a "bump" near the peak wave frequency n_0, as indicated in Figure 11.

4.4. Quadrant Analysis

Quadrant analysis is a conditional sampling technique originally developed for turbulent laboratory flows by *Lu and Willmarth* [1973]. It separates the fluxes into four categories, according to the sign of the two fluctuating components. Thus, with the two components denoted x and y and numbering the quadrants according to mathematical convention, we have for the x-y plane:

quadrant I $\quad x > 0, y > 0$

quadrant II $\quad x < 0, y > 0$

quadrant III $\quad x < 0, y < 0$

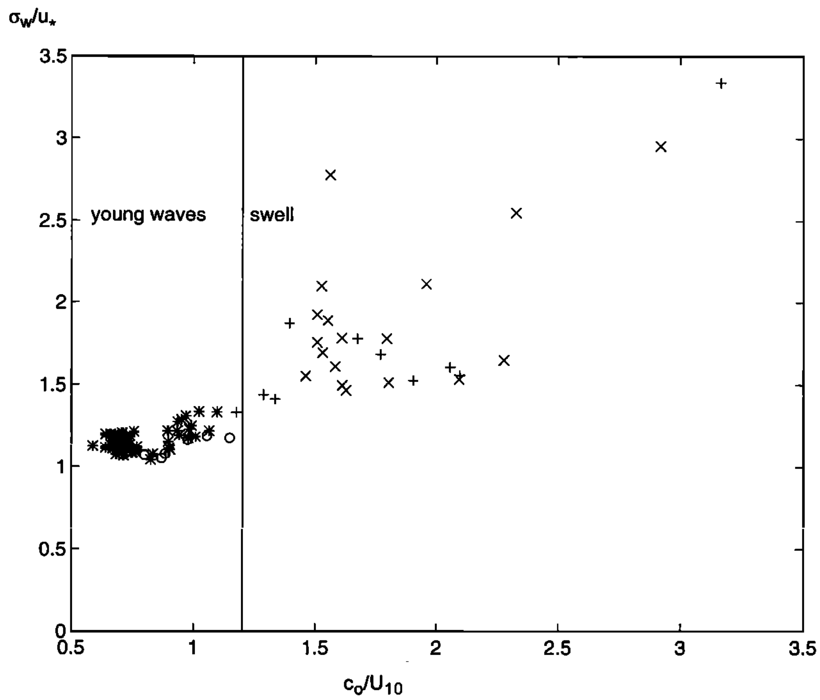

Figure 8. Normalized vertical velocity standard deviation σ_w/u_* for 10 m plotted as a function of the wave age parameter c_0/U_{10} (where c_0 has been calculated as weighted means over the flux footprint for the 10 m level, see appendix B). Circles, data from the pregale period during September 14; stars, data from the gale period September 14–17; pluses, data from September 18 and 19, with wind-wave angle difference ≤30°; crosses, same as for crosses, but with wind-wave angle difference between 30° and 60°. Note that the data set includes three additional data points with c_0/U_{10} values between 2 and 3 and σ_w/u_* between 5 and 6, i.e., out of range of the plot.

Table 2. Mean Values and Standard Deviations for σ_w/u_* for the Three Measuring Heights and for Young Waves ($c_0/U_{10} < 1.2$) and Swell ($c_0/U_{10} > 1.2$)

	10 m			18 m			26 m		
	σ_w/u_*	s.d.	N	σ_w/u_*	s.d.	N	σ_w/u_*	s.d.	N
$c_0/U_{10} < 1.2$	1.16	0.04	57	1.18	0.09	57	1.28	0.13	57
$c_0/U_{10} > 1.2$	2.15	1.02	33	1.91	0.52	33	2.84	1.42	33

N, number of measuring hours for each category.

quadrant IV $\qquad x > 0, y < 0,$

where $y = w$ and $x = u$, or θ (θ_v, actually, but for the present purpose the distinction is of little relevance) in our case. Positive contributions to the kinematic momentum flux $-u'w'$ are obtained for quadrant II events (ejections, i.e., momentum deficit being transported upward) and for quadrant IV events (sweeps, i.e., momentum excess being transported downward), whereas there are negative contributions for quadrant I (outward interaction) and quadrant III (wallward interaction). For the heat flux, $\overline{w'\theta_v'}$ quadrants I and III give positive contributions.

The importance of relatively short-lived large values of the moments $x'y'$ may be seen by estimating the importance of these events to the total flux and by comparing this with the fraction of time these large values occur. This is accomplished by determining the cumulative frequency distributions of the fluxes when keeping values larger than some given fraction of the average flux. This is equivalent to using the hyperbolic hole, introduced by *Willmarth and Lu* [1974]. The size H of the hole is defined as

$$H = |x'y'|/|\overline{x'y'}|, \tag{3}$$

where the point (x', y') lies on the hyperbola which bounds the whole region in the x-y plane. The hyperbolic hole is shown as the hatched area in Figure 12 and becomes an excluded region in the quadrant analysis. By progressively increasing the magnitude of H the importance of events exhibiting increasingly large values of $|x'y'|$ can be determined within each quadrant.

Following *Raupach* [1981], a flux fraction S_{iH}, where subscript i refers to the quadrant number, is defined as

$$S_{iH} = [x'y']_{iH}/\overline{x'y'}, \tag{4}$$

where the brackets signify a conditional average. This conditional average is formally defined using a conditioning function I_{iH} which obeys

$$I_{iH} = \begin{cases} 1, & \text{if the point } (x', y') \text{ lies in the } i\text{th quadrant and } |x'y'| \geq H|\overline{x'y'}| \\ 0, & \text{otherwise.} \end{cases}$$

Then, the conditionally averaged stress becomes

$$[x'y']_{iH} = \lim\inf \frac{1}{T}\int_0^T x'y'(t)I_{iH}(t)\,dt. \tag{5}$$

Since the stress fractions are normalized quantities, it is clear that

$$\sum_{i=1}^{4} S_{i,0} = 1. \tag{6}$$

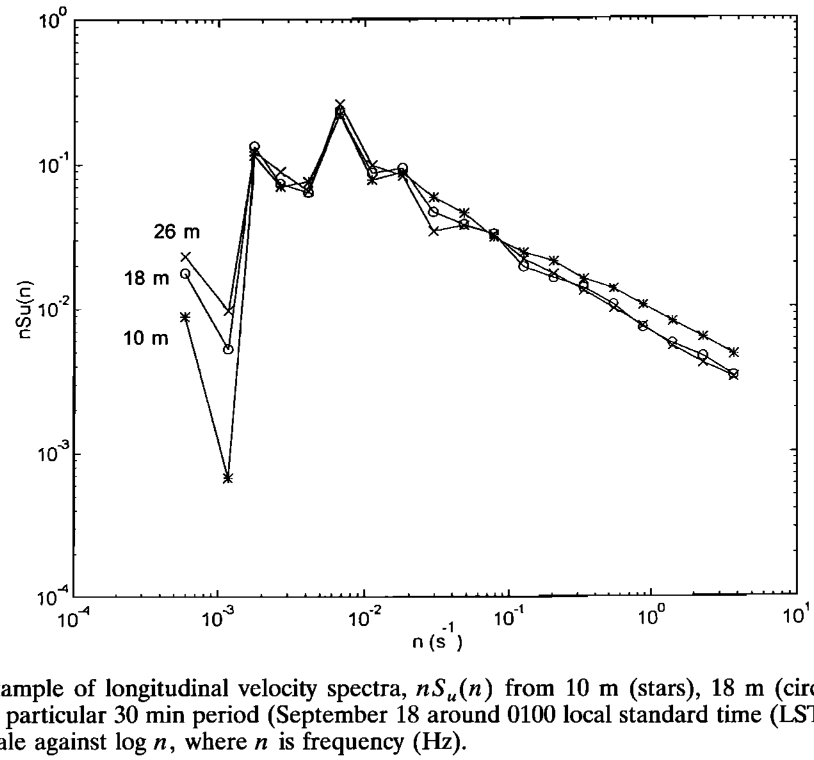

Figure 9. Example of longitudinal velocity spectra, $nS_u(n)$ from 10 m (stars), 18 m (circles), and 26 m (crosses) for a particular 30 min period (September 18 around 0100 local standard time (LST)) plotted on a logarithmic scale against log n, where n is frequency (Hz).

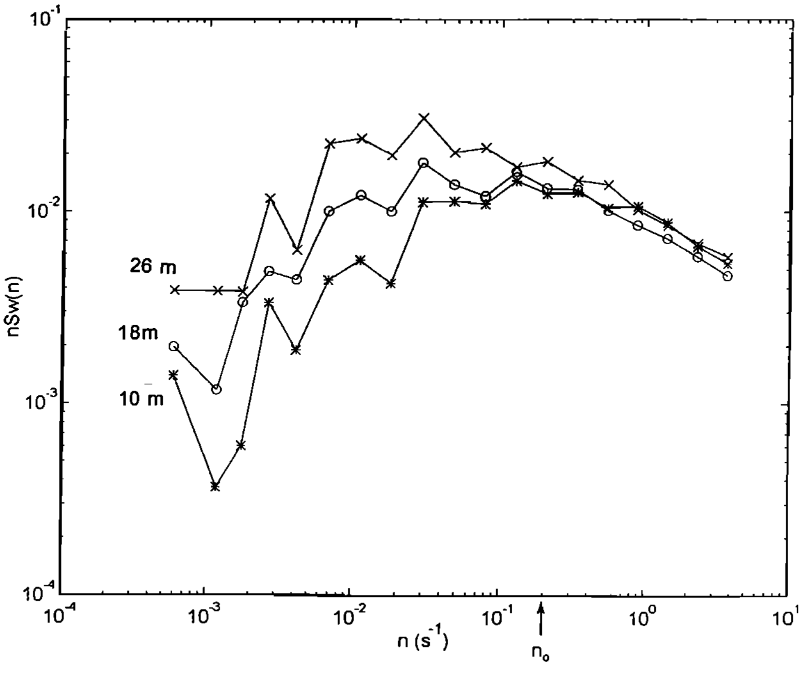

Figure 10. Example of vertical velocity spectra, $nS_w(n)$ from 10 m (stars), 18 m (circles), and 26 m (crosses), for a particular 30 min period (September 18 around 0100 LST) plotted on a logarithmic scale against log n, where n is frequency (Hz). The n_0 indicates the frequency of the peak in the wave spectrum.

Figures 13a–13d show examples of cumulative distributions in the four quadrants for $-\overline{u'w'}$ (Figures 13a and 13b) and for $\overline{w'\theta'_v}$ (Figures 13c and 13d) at the lowest measuring height, 10 m. Note that H, by definition, is always positive. This has the consequence for the composite quadrant plots of Figure 13a–13d that H increases from the center line toward the right for quadrants I and IV and toward the left for quadrants II and III. Note also that the stress fractions S_{iH} (Figures 13a and 13b) are positive for quadrants II and IV but negative for quadrants I and III. For the heat flux plots, Figures 13c and 13d, the corresponding heat flux fraction is positive for quadrants I and III and negative for quadrants II and IV.

To exemplify, take Figure 13a, which shows the momentum flux analysis for young waves, and extract first the stress frac-

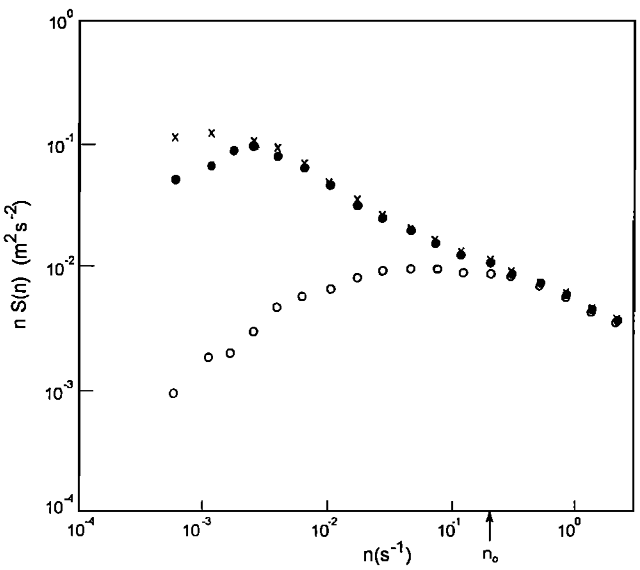

Figure 11. The 24 hour mean (from September 18, 1995) velocity spectra, $nS_{u,v,w}(n)$ for the horizontal components u (closed circles) and v (crosses) and for the vertical component w (open circles) for 10 m plotted on a logarithmic scale against log n. Also indicated in Figure 11 is the peak wave frequency n_0 during the measurement period.

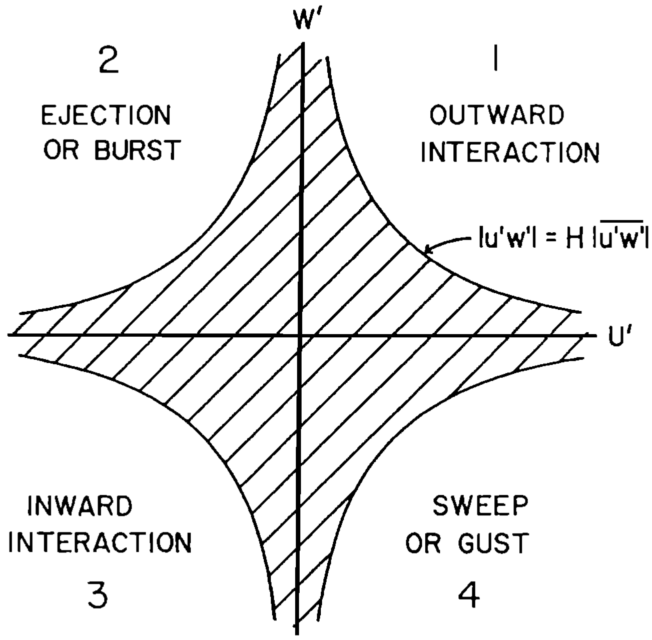

Figure 12. Longitudinal and vertical velocity fluctuation domain showing the quadrants and the hyperbolic excluded region (hatched area). H, size of the hyperbolic hole. After *Shaw et al.* [1983].

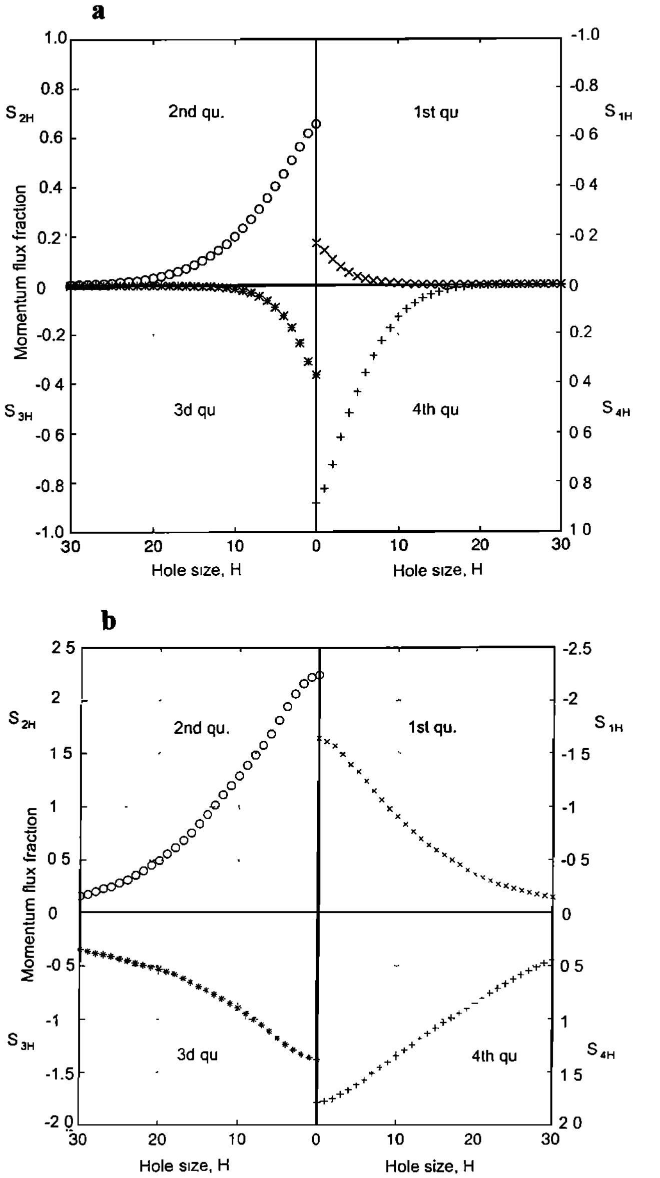

Figure 13. Examples of quadrant analysis for 10 m (a) and (c) from an hour with young waves, $c_0/U_{10} = 0.90$ (September 15, 1500 LST) and (b) and (d) from an hour with swell, $c_0/U_{10} = 3.33$ (September 18, 2000 LST). Figures 13a and 13b refer to the momentum flux and Figures 13c and 13d refer to the kinematic heat flux. Figures 13a–13d give flux fractions S_{iH}, equation (4), in the four quadrants i against hole size H, equation (3). Note that H, by definition, is positive for all quadrants and that in the momentum flux plots, Figures 13a and 13b, the sign of S_{iH} is positive for quadrants II and IV and negative for quadrants I and III and that the corresponding signs are reversed in the heat flux plots, Figures 13c and 13d.

tion values for the various quadrants for hole size $H = 0$. Figure 13a gives, approximately, $S_{1,0} = -0.17$, $S_{2,0} = 0.65$, $S_{3,0} = -0.38$, and $S_{4,0} = 0.90$, the sum of which is 1.0, as stated by (6). For $H = 10$ the corresponding approximate flux fractions are $S_{1,10} = -0.02$, $S_{2,0} = 0.20$, $S_{3,0} = -0.02$, and $S_{4,0} = 0.12$. The sum of this is 0.28, meaning that 28% of the flux occurs in events more than 10 times the average flux and that out of this, 0.2/0.28 ≈ 70% occurs in ejections, i.e., quadrant II events.

Figures 13a and 13c are from September 15, when the wind was increasing and $c_0/U_{10} = 0.90$; Figures 13b and 13d are from September 18, with $c_0/U_{10} = 3.33$. For young wave conditions the plot for $-\overline{u'w'}$ (Figure 13a) has relatively large contributions from the ejection and sweep quadrants II and IV, respectively, compared with the much smaller contributions from the interaction quadrants I and III, in general agreement with what is typically found over land. For swell conditions the $-\overline{u'w'}$ plot (Figure 13b) differs strikingly from the corresponding plot for $c_0/U_{10} = 0.90$ (Figure 13a). Thus the interaction quadrants are almost as large as the sweep and ejection quadrants. This result is in general agreement with the findings of *Chambers and Antonia* [1981]. In addition, all four curves of Figure 13b are much spread out, indicating that infrequent but intense events of fluxes of both signs play a big role in the transport process, resulting in nearly zero net flux.

The corresponding plots for the heat flux, Figures 13c and 13d, are also different from each other, but here a strong relative accentuation of the role of quadrant I results when the

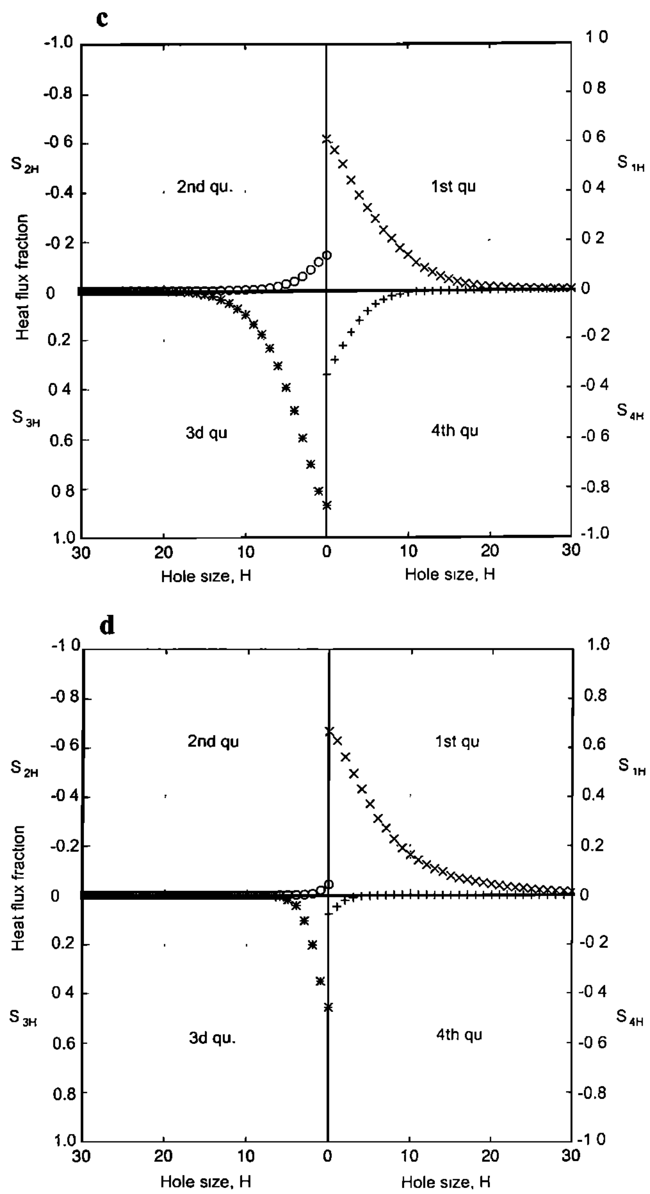

Figure 13. (continued)

Table 3. Ratios for Momentum Flux $[(\mathrm{II}+\mathrm{IV})/(\mathrm{I}+\mathrm{III})]_{Hm}$ and for Heat Flux $[(\mathrm{I}+\mathrm{III})/(\mathrm{II}+\mathrm{IV})]_{Hh}$ for 10 and 26 m and For Young Wave ($c_0/U_{10} = 0.89$) and Swell ($c_0/U_{10} = 2.04$) Conditions

Height Above Sea Level, m	H	c_0/U_{10} 0.89	c_0/U_{10} 2.04
	Momentum Flux		
10	0	3.1 ± 0.4	1.5 ± 0.3
	5	7.9 ± 2.5	1.7 ± 0.5
	10	17.6 ± 7.7	2.0 ± 0.9
26	0	2.8 ± 0.7	1.5 ± 0.5
	5	6.6 ± 3.2	1.6 ± 0.5
	10	14.6 ± 8.3	2.0 ± 1.0
	Heat Flux		
10	0	3.3 ± 0.8	8.1 ± 0.6
	5	9.3 ± 5.6	∞
	10	19 ± 12	∞
26	0	3.3 ± 0.5	6.0 ± 2.6
	5	9.4 ± 4.0	29 ± 14
	10	24 ± 13	∞

The figures are mean values, derived from hourly means for periods of ~48 hours duration each, with standard deviations. Roman numerals denote quadrant number, and H is hole size.

wave age increases. *Chambers and Antonia* [1981] observe no change in the form of their heat flux quadrant plots when their c/u_* increases from ~40 to 80, but their analysis is based on just a few cases. The pattern illustrated in Figures 13a–13d is very persistent in the present data set. This is illustrated by the analysis presented in Table 3. Shown in Table 3 are the ratios $[(\mathrm{II}+\mathrm{IV})/(\mathrm{I}+\mathrm{III})]_{Hm}$ for $-\overline{u'w'}$ and $[(\mathrm{I}+\mathrm{III})/(\mathrm{II}+\mathrm{IV})]_{Hh}$ for $\overline{w'\theta'_v}$, where roman numerals denote quadrant numbers, H is hole size, and m and h denote momentum and heat flux, respectively. All data from September 14 and 15 have been taken together in one group, having a mean value for c_0/U_{10} of 0.89, and all data from September 18 and 19 are in another group with a mean c_0/U_{10} of 2.04. Results are given for three hole sizes $H = 0$, 5, and 10.

For the momentum flux, Table 3 shows that for 10 m and $c_0/U_{10} = 0.89$ the ratio increases from ~3 to ~18 when the hole size increases from 0 to 10, whereas it is in the range between 1.5 and 2 for $c_0/U_{10} = 2.04$, thus showing the strongly increasing influence of the interaction quadrants with increasing wave age and increasing hole size. The pattern is very much the same for 26 m. For the heat flux the ratio $[(\mathrm{I}+\mathrm{III})/(\mathrm{II}+\mathrm{IV})]_{Hh}$ changes from 3 to 20 when H increases from 0 to 10 for the young wave case. For the swell case the ratio is between 6 and 8 for $H = 0$ and very large for $H \geq 5$. Also for the heat flux the pattern remains largely unchanged with height.

5. Discussion

5.1. Summary of Results

The most striking features of the present study are the following: (1) For values larger than 1.2 for the wave age parameter c_0/U_{10} the shearing stress at and near the surface becomes strongly suppressed, $-\overline{u'w'}$ taking on values smaller than 0.01 $m^2\ s^{-2}$, the corresponding average C_D value being $\sim 0.7 \times 10^{-3}$. (2) The turbulent intensities of all three velocity components remain high, so that the modulus of the correlation coefficient for u and w drops from its typical normal value of ~0.35 to a value between 0.2 and 0. (3) Most of the time there is a wind speed maximum below a height of 10 m above the mean water level, a phenomenon interpreted as a wave-driven wind speed increase. (4) The characteristic changes to the turbulence structure mentioned under feature 2 are observed equally clearly at 10 and at 18 and 26 m. (5) The turbulence energy budget at 10 m is dominated by two gain terms of approximately equal magnitude, pressure transport, and buoyancy, whereas the local mechanical production and turbulent transport terms are very small numerically. (6) Wave-related signatures in energy spectra and cospectra are not very pronounced at any of the measuring levels. (7) Quadrant analysis of the momentum flux shows that flux contributions from the interaction quadrants become almost as big as the sum of sweeps and ejections for high-wave age conditions, making the net flux numerically small; no such corresponding effect is observed in quadrant analysis of the heat flux. In that case, instead, the relative contribution of quadrant I to the transport process increases dramatically.

The above picture for the momentum flux is in general agreement with previous findings in similar situations [*Volkov*, 1970; *Makova*, 1975; *Antonia and Chambers*, 1980; *Chambers and Antonia*, 1981]. As noted in section 4, previous measurements were mainly confined to relatively low heights above the water surface, and in none of these studies were there simultaneous measurements of turbulent characteristics at several levels. Thus it is a new finding of this study that the turbulence "anomalies" during swell (compared to young wave conditions) are actually observed to occur in a layer extending to at least 26 m. In fact, there are no indications in the data of a gradual decrease of the "degree of anomaly" within this layer.

5.2. Possible Links to Processes in the Deep Boundary Layer

As mentioned in section 1, the meteorological regime studied by STH (1994) had all the characteristics of previous studies during swell conditions. There were, unfortunately, no wave measurements to confirm that, actually, $c_0/U > 1.2$. The fact that the situation occurred in the aftermath of a gale is, however, strong indirect evidence that this was actually the case.

The unique feature of the study described by STH (1994) is the occurrence of simultaneous airborne and tower-mounted measurements. During a period of ~5 hours the momentum flux was observed to be slightly positive not only in the tower measurements at a height of 22 m but throughout the lowest 100–200 m layer of the atmosphere, as revealed from flight legs at 30, 60, 90, 150, and 200 m above the water surface. Wind speed was between 2 and 3 m s^{-1} throughout the lowest 500 m. In spite of this virtual absence of shearing stress at the surface, turbulence intensity was high, giving, in fact, almost constant rate of dissipation throughout the bulk of the boundary layer or, more precisely, up to a height of 700 m.

Figure 14, which is reproduced from STH (1994), presents the terms of the turbulence energy budget for the entire boundary layer. Figure 14a shows the mechanical production term P, dissipation ε, turbulent transport term T_t, and the buoyancy production term B, whereas Figure 14b shows the imbalance term (solid curve in the right-hand part of the graph), interpreted as pressure transport T_p. Note that all terms, including the pressure transport term derived from the airborne measurements, extrapolate nicely to the independent tower measurements at 22 m.

The relative role of the various terms of the turbulence

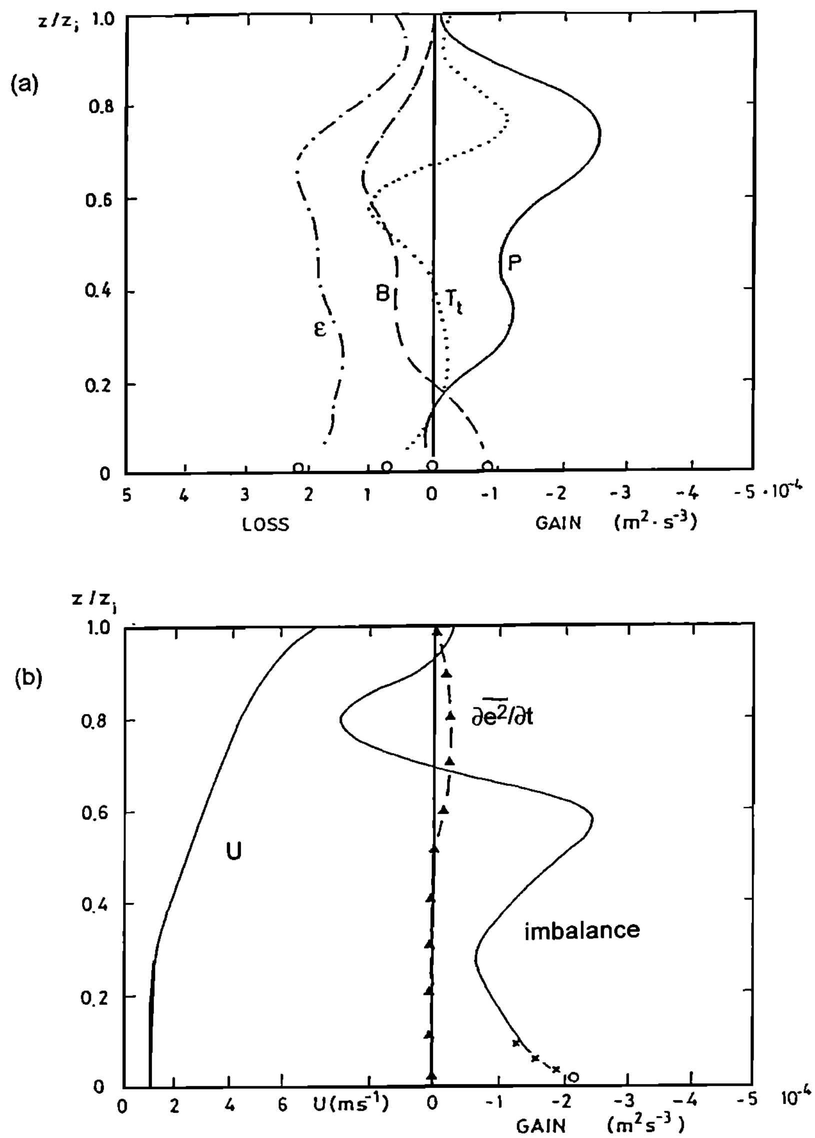

Figure 14. Turbulence energy budget estimates from the study of STH (1994). (a) Mean profiles of the various terms of the turbulence energy budget that were directly derived from airborne slant profiles (curves) and mast measurements (circles). (b) Right-hand part: imbalance obtained when summing up the directly measured terms from slant profiles (solid curve), horizontal flight legs (dashed curve with crosses), and mast measurements (circle). Dashed curve with triangles is the time rate of change term derived from profiles at 0900 and 1130 LST. Left-hand part: Mean wind profile. Same notations as in Figure 6; z_i denotes the height of the mixed layer. After *Smedman et al.* [1994].

energy budget for the layers close to the surface given by STH (1994) are very much the same as observed in the present study: Mechanical production is close to zero, which is also the case for turbulent transport. The pressure transport term and buoyancy production thus make up most of the energy gain, being balanced by dissipation. In Figure 14 it is clearly seen that the net source of turbulent energy is mechanical production in the upper half of the boundary layer; buoyancy production, which is a gain near the surface, being a loss throughout the bulk of the boundary layer.

The turbulence characteristics of the boundary layer studied by STH (1994) bear all the characteristics of a convectively mixed boundary layer [*Kaimal et al.*, 1976]. However, the similarity is only formal, with the height of the boundary layer z_i being the characteristic length scale. It was shown that this boundary layer is not driven by thermal convection but by large-scale turbulence that was produced in the upper layers in the boundary layer and brought down to lower heights by the pressure transport mechanism. It was argued that this phenomenon must be identical to inactive turbulence, which was first identified by *Townsend* [1961] and *Bradshaw* [1967] in laboratory flow. *Högström* [1990] showed that inactive turbulence is likely to be universally present in near-neutral atmospheric boundary layer flow (explaining, e.g., why the correlation coefficient between u and w in the near-neutral atmospheric surface layer is about -0.35 rather than -0.5 as typically found in turbulent laboratory boundary layer flow).

As the concept of active and inactive turbulence is crucial to the interpretation of the present flow regime, a brief summary of the general characteristics of these phenomena is given here. *Townsend* [1961, p. 116] introduced the concept of active and inactive turbulence in a boundary layer thus: "(i) Active turbulence which is responsible for the turbulent transfer and determined by the stress distribution and (ii) an inactive component which does not transfer momentum or interact with the universal component." Inactive turbulence is characterized by the following: (1) It does not interact with the active turbulence in the inner layer (the surface layer). (2) It does not contribute to the shearing stress. (3) It arises in the upper part of the boundary layer. (4) It is of relatively large scale. (5) It is partly due to the irrotational field created by pressure fluctuations in the boundary layer and partly due to the large-scale vorticity field of the outer layer seen as an unsteady external stream.

Note that in a flow situation where inactive turbulence becomes of major importance the surface momentum flux drops while turbulence intensity remains high. This will result in reduction of the correlation coefficient between the u and w component, $-r_{uw}$, as observed (Figure 7), and an increase of normalized velocity standard deviations, as illustrated in Figure 8 for σ_w/u_* but also noted for the two normalized horizontal wind components.

The following main conclusion was drawn by STH (1994) concerning the mechanism of inactive turbulence: The net energy exchange at the surface is such that the surface shearing stress is close to zero. In keeping with the conclusion from the community-wide evaluation of turbulent boundary layers [*Kline and Robinson*, 1989] that turbulence production close to the surface is an autonomous process that takes place largely independent of large-scale processes in the outer layer it was argued that the turbulence observed near the surface was in fact just inactive turbulence, "imported" from above by pressure transport. As a contrast, the "traditional view," expressed, e.g., by *Kitaigorodskii* [1973] as well as by *Antonia and Chambers* [1980] concerning the observed combination of numerically very small values of momentum flux and relatively large values of the turbulent fluctuations, is that this state of affairs is brought about by pressure transport of momentum upward from the waves to the atmosphere. Below, an attempt will be made to reconcile these two seemingly contrasting views of the turbulence mechanism above a surface with waves traveling faster than the wind.

5.3. A Conceptual Model of the Turbulence Regime Above a Surface With Waves Travelling Faster Than the Wind

Return to the spectral graphs of the longitudinal wind component and note the following: (1) From the individual examples of simultaneous spectra at 10, 18, and 26 m in Figure 9 it is clear that these spectra do not scale with height. The same result was obtained throughout the swell period. (2) From the 24 hour mean u spectrum displayed in Figure 11 it is clear that the peak is found at a frequency as low as 10^{-3} Hz. This contrasts sharply with the wave spectrum peak which is found around 0.2 Hz. In fact, the shape of the u spectrum in Figure 11 is very similar to that observed by STH (1994) throughout the lowest 300 m (STH, 1994, Figure 5a), the main difference being the slight bulge noticeable in the 10 m spectrum in Figure 11 near the peak wave frequency. Spectra of the lateral component have the same characteristics as the u spectrum: independence of height and with a peak frequency around 10^{-3} Hz as well as striking similarity with corresponding spectra observed by STH (1994, Figure 5b).

Figure 10 shows an example of simultaneous w spectra at the three measuring heights of the present study. As noticed earlier, the spectral curves collapse in the high-frequency range but diverge in the low-frequency range, with spectral levels increasing with height. Comparison with the corresponding w spectra from STH (1994, Figure 5c) shows exactly analogous behavior throughout the lowest 300 m. The frequency of the spectral peak at the lowest measuring height in that study, 22 m, corresponds quite well with that observed at 26 m in the present study. In fact, the above spectral behavior is exactly what is expected for a boundary layer dominated by inactive turbulence, which, in turn, bears striking resemblance to a convective boundary layer. Thus, as explained by STH (1994), the spectra of the horizontal components remain largely the same over a large portion of the boundary layer whereas the spectra of the vertical component change systematically with height in such a manner that the spectral maximum shifts to progressively lower frequencies with height. Note that the similarity with a convective boundary layer is only formal, as discussed below.

In the discussion of the turbulence energy budget at 10 m in section 4 it was noted that buoyancy production was of the same magnitude as the pressure transport gain. Thus it is a relevant question whether the boundary layer of the present study is in fact dominated by buoyancy instead of, as suggested, by inactive turbulence. Also, in the case of STH (1994), buoyancy production occurred in the layers near the surface (Figure 14a). This term changes sign already at ~200 m, and it was shown by STH (1994) that spectral scaling was not in agreement with the idea of mixed layer scaling. Thus observations of *Kaimal et al.* [1976] show that the ratio of dissipation to buoyancy production is constant with height in the convective boundary layer: $\Psi = \varepsilon/[(g/T_0)(w'\theta')_0] \approx 0.6$. For the present study, $\Psi \approx 1.7$, which is not far from the value reported by STH (1994, p. 3405), "around 2." This analysis shows conclusively that mixed layer scaling is not applicable here. Another consequence is also evident: As the boundary layer is controlled by an entirely different turbulence mechanism than is usually the case, we cannot expect Monin-Obukhov scaling to be valid.

The result shown in Figure 13d for the heat flux during swell is in remarkable agreement with the large eddy simulations (LES) of *Khanna and Brasseur* [1998] of the expected values of $w'\theta'$ conditioned on w' for the simulated convective boundary layer [*Khanna and Brasseur*, 1998, Figures 26 and 28]. Khanna and Brasseur find both for the very unstable case (characterized by $z_i/L = -730$, where z_i is the height of the convective boundary layer and L is the Monin-Obukhov length) and the slightly unstable case ($z_i/L = -8$) that the heat flux is strongly dominated by upward directed motions, at least for heights $>0.1\ z_i$. Again we see striking similarity between the swell boundary layer, which is controlled by inactive turbulence, and the ordinary convective boundary layer.

To conclude, in the lowest layers of the near-neutral marine atmospheric boundary layer during swell conditions, both buoyancy and shear production are small, leaving pressure transport as the dominant source of turbulent energy. This energy is fed into the vertical component and redistributed to the horizontal components by pressure-velocity derivative correlations. This means that the "swell boundary layer" has certain characteristics in common with a free-convection boundary layer, because shearing stress is quite small and the energy input is in the vertical component.

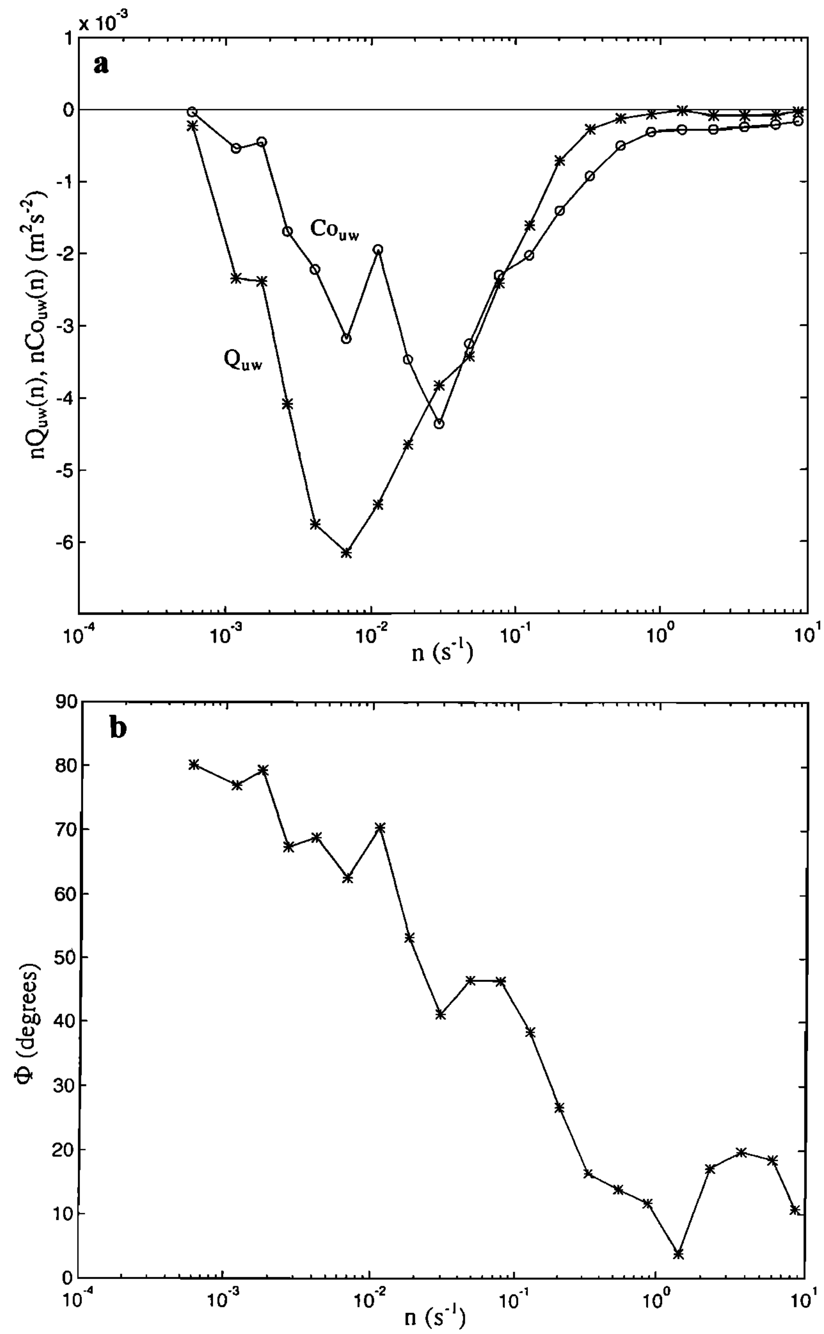

Figure 15. (a) Mean u, w cospectra (curves with circles) and quadrature spectra (curves with stars) for September 18, 1995, 10 m, and (b) the corresponding phase angle ϕ as function of frequency.

Figure 15a shows mean cospectra and quadrature spectra $\mathrm{Co}_{uw}(n)$ and $Q_{uw}(n)$, respectively, calculated for the entire September 18, and Figure 15b shows the corresponding phase angle ϕ for the same period, determined from the relation [see, e.g., *Lumley and Panofsky*, 1964]

$$\tan \phi = Q_{uw}(n)/\mathrm{Co}_{uw}(n). \tag{7}$$

The systematic increase of phase angle with decreasing frequency displayed in Figure 15b is in striking contrast to the corresponding plots for the pre-swell days which show near-zero phase angle for frequencies below $\sim 10^{-2}$ Hz (not shown here). It is notable that the phase angle in Figure 15b comes close to 90° for the lowest frequencies; that is, u and w become completely out of phase, giving zero contribution to the cospectrum and thus to the momentum flux, in exact agreement with the prediction for inactive turbulence, which we expect to find at these low frequencies. Note that the phase angle is ≥60° for frequencies below $\sim 10^{-2}$ Hz. This is an indication that in the frequency range $10^{-3} \leq n \leq 10^{-2}$ there is a mixture of truly inactive turbulence, which has a phase angle of 90°, and active turbulence with phase angle zero. Analysis of cospectra and quadrature spectra and the corresponding phase angle for vertical velocity and temperature (not shown here) for the same time period (September 18) reveals an entirely different behavior, i.e., a phase angle that fluctuates randomly around zero over the entire frequency domain encountered.

From comparison of spectra from the present study and those from STH (1994) the following conclusions can be drawn: (1) It is quite reasonable to assume that the same mechanism created the observed turbulence features in the two studies. (2) It is highly unlikely that this turbulence has been produced by influence from the waves. Instead, it is very probable that inactive turbulence produced aloft has been brought down to near the surface by pressure transport. The crucial question then becomes the following: How does the air-sea interaction process come into the picture?

It is reasonable to assume that in a shallow layer just above the undulating water surface there is, in the terminology of *Belcher and Hunt* [1993], an inner surface layer, which is governed by local momentum transfer in the direction from the air to the sea. In this layer it is also reasonable to assume that the ordinary wall layer turbulence production mechanism is active [*Kline and Robinson*, 1989]. At the same time, the longer waves (which travel faster than the wind) produce momentum transport by pressure fluctuations in the opposite direction. That such transport actually takes place is clearly demonstrated by the quadrant analysis, which shows that for the momentum transport the interaction quadrants become of increasing importance with increasing wave age; that is, excess momentum is being transported upward and deficit momentum is being transported downward. At the same time, the heat flux is not at all affected in this way. Thus momentum must be transported upward from the surface by a mechanism which includes pressure-velocity correlations. Such a mechanism is not possible for transport of a scalar, such as virtual potential temperature, which is studied here.

This situation creates a net momentum transport that is close to zero. This in turn means that there can be little local mechanical production of turbulence (because mechanical production is equal to the product between the kinematic momentum flux and the local wind gradient). The net result of this state of affairs is that, in fact, there will be little active turbulence in the boundary layer, except in a shallow inner surface layer near the undulating water surface, leaving primarily the inactive kind of turbulence, which is likely to originate, primarily, high up in the boundary layer. It is worth noting that during the present situation with swell, the number of individual 60 min periods with negative net momentum flux (upward directed flux) increases with height, being zero at 10 m, 3 at 18 m, and 6 at 26 m. In the case studied by STH (1994) the net momentum flux was found to be slightly negative in the lowest 200 m during a period of several hours.

The above sketch does not answer the question of how deep the zone of direct wave influence is and how deep the inner surface layer is. The measurements of this study do not give very clear surface wave signatures in the spectra during the swell period: At the most there is a bulge and a plateau in the mean u and w spectra displayed in Figure 11. At the same time, as shown in Figure 4, there is a wind maximum present somewhere below the lowest measuring point, 10 m, for most of the time during the swell period. From that it can be concluded that the inner surface layer is certainly <10 m deep. A way of describing the situation would be to say that the bulk of the boundary layer is floating with very little friction on top of a layer limited in depth by this wind maximum close to the surface.

5.4. Generality of the Present Results

The situation that has been the subject of the present study is very well defined: It occurred in the aftermath of a gale, so there was a wind speed drop from ~15 m s^{-1} to 4 m s^{-1} over a period of about a day; during a period of 48 hours after this wind speed drop occurred, the wind direction fluctuated within a ±50° sector, and the wind speed was rather constant; the wave spectrum had a single peak, and the direction of the waves was roughly the same as that of the wind; and the swell originated from an area with stronger winds located in the southernmost part of the Baltic Sea. From the information available for the cases with strong frictional decoupling reported in section 1 it appears that similar conditions prevailed in these cases as well. As revealed by Figures 7a and 8, no systematic differences were found in statistics derived separately for periods when wind and wave directions were within 30° of each other and when they differed by between 30° and 60°, respectively.

It is interesting to ask what the requirements are for a situation similar to this to occur, in terms of wind speed drop, alignment of wave propagation and wind, and, not the least, timescale of the driving forces producing this situation. To be more precise: Does a similar reduction of stress as that observed here occur as soon as there is an appreciable drop in wind speed; does it occur in a situation with a multipeak wave spectrum? At present there appears to be no information available to answer these and related questions concerning the generality of the results discussed here. One may speculate that effects of this kind occurring during less well pronounced conditions could temporarily reduce the stress and thus contribute to the inevitable scatter of C_D plots (a hysteresis effect similar to that displayed in Figure 5 for the wind gradient). It is also relevant to ask what the requirements are for frictional reduction to occur in open ocean areas; is the situation occurring as regularly as there are appreciable wind speed drops after the passage of storms, or does omnidirectional swell change the situation to a considerable degree?

6. Conclusions

A case has been studied which is characterized by the dominant waves traveling faster than the wind. It has been demonstrated that at the same time as momentum is transported from the atmosphere to the ocean surface by the ordinary turbulent mechanism, momentum is also transferred from the waves to the atmosphere by the pressure transport term, producing a wave-driven wind increase at low height (a consistent wind speed maximum below 10 m) and very low net surface shearing stress. It was observed that turbulence intensities were nevertheless quite high at 10, 18, and 26 m above the surface, giving a u, w correlation coefficient with a modulus in the range 0 to 0.2. Direct wave signatures in the wind spectra are quite weak. It is concluded that mechanical turbulence production in the layer covered by the observations is virtually zero. Instead, the turbulence energy must have been brought down by pressure transport from layers in the upper parts of the boundary layer, so-called inactive turbulence. Analyses of turbulence characteristics reveal that a systematic change occurs at wave age $c_0/U_{10} = 1.2$, indicating an almost discontinuous change of regime.

Appendix A: Determination of Flux Footprint for the Eddy Correlation Measurements at Östergarnsholm

The turbulent flux measured at some height on the Östergarnsholm tower originates from an upwind area at some distance from the tower. It is the purpose of appendix A to show how the location of this area, "the flux footprint," for the three measuring heights 10, 18, and 26 m above mean sea level was determined.

It is assumed that the flux originates at the surface from a row of infinitely wide line sources oriented perpendicular to the mean wind direction during a particular run. The source strength is assumed to equal $Q(x)$ with units kg m^{-2} s^{-1}. Assuming stationary conditions and that the flux gradient relationship holds, the diffusion equation takes the form:

$$\frac{\partial}{\partial z}\left(K_z \frac{\partial \bar{\chi}}{\partial z}\right) + \bar{u}\,\frac{\partial \bar{\chi}}{\partial x} = 0. \tag{A1}$$

Here K_z is the exchange coefficient, $\bar{\chi}$ is the mean concentration, and u is the mean wind speed. For neutral conditions, $K_z \approx u_* kz$ and $\bar{u} = u_*/k \ln z/z_0$, and (A1) cannot be solved analytically. An approximate solution of this equation was, however, obtained by *van Ulden* [1978]. *Gryning et al.* [1983] carried out numerical solutions, which were found to be in close agreement with those of *van Ulden* [1978] and in very good agreement with measurements from Project Prairie Grass. Gryning et al. find that the solution can be approximated with the following expression:

$$\bar{\chi}(x, z) = \frac{Q}{A'(s)u_{px}\sigma_z} \exp\{-[z/B'(s)\sigma_z]^s\}, \tag{A2}$$

where u_{px} is the mean wind speed at the height $0.6\,\bar{Z}$, where $\bar{Z}(x)$ is the height of the plume center line, $\sigma_z \approx 1.35\,\bar{Z}$, for neutral conditions and s is a parameter which can take on values between 0.5 and ~2.7 depending on stability and distance from the source. For neutral stratification, *Gryning et al.* [1983] found that $s \approx 1.25$. For this value, *van Ulden* [1978] finds $A' = 0.902$ and $B' = 0.968$.

van Ulden [1978] presents the following expression for neutral conditions:

$$x/z_0 = \frac{0.74}{\kappa^2}\frac{\bar{Z}}{z_0} \ln\left(0.6\,\frac{\bar{Z}}{z_0}\right). \tag{A3}$$

Taking $z_0 = 1.5 \times 10^{-4}$ m as a typical value for the roughness length over sea, x can be computed as a function of $\bar{Z}$. Plotting the result in a log-log representation shows that the data fall closely on a straight line, which corresponds to

$$\bar{Z} = 2.22 \times 10^{-2}(x^{0.94}) \tag{A4}$$

From *van Ulden* [1978] it also follows that for neutral conditions

$$\bar{\chi}(x, 0)u_*/Q \approx 1.54/x. \tag{A5}$$

The vertical flux at the point (x, z) is

$$F(x, z) = -K_z(\partial\bar{\chi}/\partial z)(x, z) \approx -kzu_*(\partial\bar{\chi}/\partial z)(x, z) \tag{A6}$$

The derivative $\partial\bar{\chi}/\partial z$ is obtained after differentiation of (A2). Inserting the ensuing expression in (A6), together with (A3) and (A4) and the values for s, A', and B' outlined above gives the following approximate expression for neutral conditions:

$$F(x, z)/Q = \frac{0.674}{x}\left[\frac{z}{3.0 \times 10^{-2}(x^{0.94})}\right]^{1.25} \cdot \exp\left\{-\left[\frac{z}{3.0 \times 10^{-2}(x^{0.94})}\right]^{1.25}\right\}. \tag{A7}$$

The total vertical flux at (x, z) is the integral of $F(x, z)$ over x from zero to infinity. By numerical calculation with (A7) it is simple to obtain an approximate estimate of the flux contribution from a strip of width Δx situated between x and $x + \Delta x$. By accumulating flux contributions $\delta F(x)$ from $x = 0$ to increasing distances in the wind direction it is possible to calculate the relative role of upwind areas at different distances in the total measured flux.

It is found from such calculations that for the 10 m level, 90% of the measured flux originates from areas beyond 250 m and 50% originates from beyond 670 m and that 70% of the flux comes from areas between 250 and 1700 m. For 18 m the corresponding figures are 450 m, 1250 m, and 450 and 3200 m, respectively. For 26 m, finally, the corresponding figures are 770 m, 1980 m, and 770 and 5300 m.

The above calculations refer to an ordinary neutral surface layer. In this study, particular interest is focused on the swell situation. As discussed in this paper, the turbulence structure in this case differs from that of the ordinary case. At this moment there is hardly enough information to tailor the footprint equations to fit exactly this kind of situation. Generally speaking, C_D was found to be reduced compared to the ordinary case during swell. This means that the effective roughness length z_0 is likely to be appreciably smaller than assumed in the above calculations (1.5×10^{-4} m). This, in turn, is likely to have the effect on the footprint that it becomes removed even farther from the shore compared to what was obtained from the detailed calculations.

Appendix B: Determination of the Effects of Water Depth in the Footprint for the Eddy Correlation Measurements at Östergarnsholm

To quantify the influence of shallow water, we have defined a weighted mean phase speed

$$\langle c_0 \rangle = \int_0^\infty F(x, z)c_0(x)\,dx$$

over the footprint. The weighting function is the vertical flux density $F(x, z)$ given by (A7) in appendix A, normalized so that

$$\int_0^\infty F(x, z)\,dx = 1.$$

The phase speed has been calculated using the dispersion relation

$$c_0 = \frac{g}{\omega_0}\tanh\left(\frac{\omega_0 h}{c_0}\right),$$

where ω_0 is the frequency of dominating waves (the peak of the wave spectrum) and h is the depth. The results are shown in Figure 2c for the flux footprint for 10 m (circles) and 26 m (crosses), together with the phase speed in deep water (stars).

These values can be compared with the results of *Anctil and Donelan* [1996], who have measured the effects in turbulent fluxes induced by shoaling waves. From their run 166, in which no shoaling effects can be seen in the wave height or the drag coefficient, we calculated c_0 over the footprint to vary between 79 and 91% of the deep-water value.

In our data, during the swell period the values were consistently closer to the deep-water phase speed over all three footprints. Over the footprint corresponding to the lowest 10 m elevation, c_0 varied between 92 and 99% of the deep-water value (Figure 2c). Over the footprint corresponding to 26 m, c_0/c_{deep} was between 99 and 100%.

During *Anctil and Donelan*'s [1996] run 166 the peak wave period T_0 was 5.7–6.1 s, and the significant wave height H_s was 0.8 m, which are comparable to our values; The ratio H_s/λ_0 (where λ_0 is the wavelength of waves having period T_0) was higher in their data than in our data.

In our data the values of H_s and H_s/λ_0 over different parts of the footprint were consistently smaller. Therefore no shallow-water effects can be expected to be seen in our flux data from the swell period.

On the other hand, during the gale before the swell period a significant portion of the flux at 10 m height originates from the part of the footprint where the principal wave components are influenced by the bottom. The weighted mean c_0 over the footprint corresponding to the lowest 10 m level varied between 77 and 94% of the deep-water value (Figure 2c). Since this is only slightly less than the range 79–91%, where no effects were found by *Anctil and Donelan* [1996], and significantly above the range 69–89%, where clear shoaling effects were measured both in wave steepness and in drag coefficient, we do not expect the shallow-water effects at our lowest level to be as strong as those observed by Anctil and Donelan. Our higher levels should be free from shallow-water effects: The corresponding range of c_0/c_{deep} is 86–97% at 18 m level and 90–99% at 26 m level.

Before the gale, c_0/c_{deep} was as high as 94–95% over the footprint corresponding to the lowest level, and therefore the fluxes during that time should not be influenced by shallow water effects. These points (circles) can hardly be distinguished from the other tightly clustered pre-swell values in Figures 7a and 8. Therefore, even during the gale, the shallow-water effects seem small at all elevations.

Acknowledgments. The costs for establishing the Östergarnsholm field station were defrayed by grants from the Natural Science Research Council (NFR) contract G-AA/GU 03556-313 and from the Swedish National Energy Administration, grant 506 226-4. The work of the first author was made possible by a grant from NFR contract S-AA/FO 03556-314.

References

Anctil, F., and M. A. Donelan, Air-water momentum flux observations over shoaling waves, *J. Phys. Oceanogr.*, *26*, 1344–1353, 1996.

Antonia, R. A., and A. J. Chambers, Wave-induced disturbances in the marine surface layer, *J. Phys. Oceanogr.*, *10*, 611–622, 1980.

Belcher, S. E., and J. C. R. Hunt, Turbulent shear flow over slowly moving waves, *J. Fluid Mech.*, *251*, 109–148, 1993.

Benilov, A. Yu., O. A. Koutznetsov, and G. N. Panin, On the analysis of wind wave-induced disturbances in the atmospheric surface layer, *Boundary Layer Meteorol.*, *6*, 269–285, 1974.

Bradshaw, P., "Inactive" motion and pressure fluctuations in turbulent boundary layers, *J. Fluid Mech.*, *30*, part 2, 241–258, 1967.

Chambers, A. J., and R. A. Antonia, Wave-induced effect on the Reynolds shear stress and heat flux in the marine surface layer, *J. Phys. Oceanogr.*, *11*, 116–121, 1981.

Davidson, K. L., and A. J. Frank, Wave-related fluctuations in the airflow above natural waves, *J. Phys. Oceanogr.*, *3*, 102–119, 1973.

Depuis, H., P. K. Taylor, A. Weil, and K. Katsaros, Inertial dissipation method applied to derive turbulent fluxes over the ocean during the SOFIA/ASTEX and SEMAPHORE experiments with low to moderate wind speeds, *J. Geophys. Res.*, *102*, 21,115–21,129, 1997.

Donelan, M., Air-sea interaction, in *The Sea*, vol. 9, *Ocean Engineering Science*, pp. 239–292, Wiley-Interscience, New York, 1990.

Grelle, A., and A. Lindroth, Flow distortion by a Solent sonic anemometer: Wind tunnel calibration and its assessment for flux measurements over forest and field, *J. Atmos. Oceanic Technol.*, *11*, 1529–1542, 1994.

Gryning, S.-E., A. P. van Ulden, and S. Larsen, Dispersion from a continuous ground-level source investigated by a K-model, *Q. J. R. Meteorol. Soc.*, *109*, 355–364, 1983.

Harris, D. L., The wave-driven wind, *J. Atmos. Sci.*, *23*, 688–693, 1966.

Högström, U., Non-dimensional wind and temperature profiles in the atmospheric surface layer: A re-evaluation, *Boundary Layer Meteorol.*, *42*, 55–78, 1988.

Högström, U., Analysis of turbulence structure in the surface layer with a modified similarity formulation for near neutral conditions, *J. Atmos. Sci.*, *47*, 1949–1972, 1990.

Kaimal, J. C., J. C. Wyngaard, Y. Izumi, and O. R. Coté, Spectral characteristics of surface layer turbulence, *Q. J. R. Meteorol. Soc.*, *98*, 563–589, 1972.

Kaimal, J. C., J. C. Wyngaard, D. A. Haugen, O. R. Coté, Y. Izumi, S. J. Caughey, and C. J. Readings, Turbulence structure in the convective boundary layer, *J. Atmos. Sci.*, *33*, 2152–2169, 1976.

Khanna, S., and J. G. Brasseur, Three-dimensional buoyancy- and shear-induced local structures of the atmospheric boundary layer, *J. Atmos. Sci.*, *55*, 710–743, 1998.

Kitaigorodskii, S. A., *The Physics of Air-Sea Interaction*, Engl. Transl., 237 pp., Gidrometeorol. Izdatel'stvo Leningrad, 1973.

Kline, S. J., and S. K. Robinson, Quasi-coherent structures in the turbulent boundary layer, I, Status report on a community-wide summary of the data, in *Zoran Zaric Memorial International Seminar on Near-Wall Turbulence, Dubrovnik, Croatia*, pp. 200–217, Hemisphere, New York, 1989.

Lai, R. J., and O. H. Shemdin, Laboratory investigation of air turbulence above simple water waves, *J. Geophys. Res.*, *76*, 7334–7350, 1971.

Lu, S. S., and W. W. Willmarth, Measurements of the structure of the Reynolds stress in a turbulent boundary layer, *J. Fluid Mech.*, *60*, 481–511, 1973.

Lumley, J. L., and H. A. Panofsky, *The Structure of Atmospheric Turbulence*, 239 pp., Wiley-Interscience, New York, 1964.

Lundin, K., A. Smedman, and U. Högström, A system for wind and turbulence measurements in a wind farm, paper presented at European Community Wind Energy Conference, Madrid, September 10–14, 1990.

Makova, V. I., Features of the dynamics of turbulence in the marine atmospheric surface layer at various stages in the development of waves, *Izv. Acad. Sci. USSR Atmos. Oceanic Phys.*, Engl. Transl., *11*, 177–182, 1975.

Monin, A. S., and A. M. Yaglom, *Statistical Fluid Mechanics*, vol. 1, 769 pp., MIT Press, Cambridge, Mass., 1971.

Pierson, W. J., Jr., and L. Moskowitz, A proposed spectral form for fully developed wind seas based on the similarity theory of S. A. Kitaigorodskii, *J. Geophys. Res.*, *69*, 5181–5190, 1964.

Raupach, M. R., Conditional statistics of Reynolds stress in rough-wall and smooth-wall turbulent boundary layers, *J. Fluid Mech.*, *108*, 363–382, 1981.

Shaw, R. H., J. Tavangar, and D. P. Ward, Structure of the Reynolds stress in a canopy layer, *J. Clim. Appl. Meteorol.*, *22*, 1922–1931, 1983.

Smedman, A.-S., M. Tjernström, and U. Hogström, The near-neutral marine atmospheric boundary layer with no surface shearing stress: A case study, *J. Atmos. Sci.*, *51*, 3399–3411, 1994.

Townsend, A. A., Equilibrium layers and wall turbulence, *J. Fluid Mech.*, *11*, 97–120, 1961.

van Ulden, A. P., Simple estimates for vertical diffusion from sources near the ground, *Atmos. Environ.*, *12*, 2125–2129, 1978.

Volkov, Yu. A., Turbulent flux of momentum and heat in the atmospheric surface layer over a disturbed sea-surface, *Izv. Acad. Sci. USSR Atmos. Oceanic Phys.*, Engl. Transl., *6*, 770–774, 1970.

Willmarth, W. W., and S. S. Lu, Structure of the Reynolds stress and the occurrence of bursts in the turbulent boundary layer, *Adv. Geophys.*, *18A*, 287–314, 1974.

H. Bergström, U. Högström, A. Rutgersson, and A. Smedman, Department of Earth Sciences, Meteorology, Villavägen 16, S-752 36 Uppsala, Sweden. (Ann-Sofi.Smedman@met.uu.se)

K. K. Kahma and H. Petersson, Finnish Institute of Marine Research, Helsinki, Finland.

(Received July 24, 1998; revised June 2, 1999;
accepted July 13, 1999.)